Noname manuscript No.
(will be inserted by the editor)

Stochastic nonlinear model for somatic cell population dynamics during ovarian follicle activation

Frédérique Clément · Frédérique Robin · Romain Yvinec

Received: date / Accepted: date

Abstract In mammals, female germ cells are sheltered within somatic structures called ovarian follicles, which remain in a quiescent state until they get activated, all along reproductive life. We investigate the sequence of somatic cell events occurring just after follicle activation. We introduce a nonlinear stochastic model accounting for the joint dynamics of two cell types, either precursor or proliferative cells. The initial precursor cell population transitions progressively to a proliferative cell population, by both spontaneous and self-amplified processes. In the mean time, the proliferative cell population may start either a linear or exponential growing phase. A key issue is to determine whether cell proliferation is concomitant or posterior to cell transition, and to assess both the time needed for all precursor cells to complete transition and the corresponding increase in the cell number with respect to the initial cell number. Using the probabilistic theory of first passage times, we design a numerical scheme based on a rigorous Finite State Projection and coupling techniques to assess the mean extinction time and the cell number at extinction time. We also obtain analytical formulas for an approximating branching process. We calibrate the model parameters using an exact likelihood approach using both experimental and in-silico datasets. We carry out a comprehensive comparison between the initial model and a series of submod-

Frédérique Clément
Inria, Université Paris-Saclay
LMS, Ecole Polytechnique, CNRS, Université Paris-Saclay
E-mail: frederique.clement@inria.fr

Frédérique Robin
Inria, Université Paris-Saclay
LMS, Ecole Polytechnique, CNRS, Université Paris-Saclay
E-mail: frederique.robin@inria.fr

Romain Yvinec
PRC, INRA, CNRS, IFCE, Université de Tours, 37380 Nouzilly, France
E-mail: romain.yvinec@inra.fr

els, which help to select the critical cell events taking place during activation. We finally interpret these results from a biological viewpoint.

Keywords stochastic cell population model · first passage time · finite state projection · stochastic coupling techniques · maximum likelihood estimate · embedded Markov chain

Mathematics Subject Classification (2010) 60J85 · 60J28 · 92D25 · 62M05

1 Introduction

In mammals, the number of oocytes (egg cells) available for a female throughout her reproductive life is fixed once for all, during the fetal or perinatal period Monniaux et al. (2018). Dormant oocytes are sheltered within somatic structures called ovarian follicles, which remain in a quiescent state until they get activated and undergo a longstanding process of growth and maturation ending by ovulation (release of a fertilizable oocyte). Growth initiation is asynchronous among follicles, so that all developmental stages can be observed in the ovaries at a given time, and follicles can remain quiescent for as long as tens of years Reddy et al. (2010).

In the earliest stages of development, ovarian follicles are made up of the oocyte and a single layer of surrounding somatic cells. The initial cell number is on the order of ten or several of tens according to the species and is quite variable between follicles. Such a variability is inherited from the mechanism underlying the formation of primordial follicles Monniaux (2018); Sawyer et al. (2002), which assemble from the fragmentation of multi-oocyte structures (the germ cell cysts) and retrieve more or less (somatic) cells.

The activation of primordial (quiescent) follicles is characterized by three main processes Picton (2001): (i) an irreversible transition of the somatic cell phenotypes, characterized by a change in their shape, from flattened (precursor cells) to cuboidal (proliferative cells); (ii) an increase in the number of somatic cells by cell division and (iii) the awakening and associated enlargement of the oocyte. The activation phase is ended when all somatic cells have transitioned, at which time the mono-layer developmental stage is completed, and somatic cells will go on proliferating and build up several concentric layers Fortune (2003).

In this work, we focus on the sequence of events occurring just after the initiation of follicle growth. A key issue is to determine whether cell proliferation is concomitant or posterior to cell shape change, and to assess both the time needed for all precursor cells to complete transition and the corresponding increase in the cell number with respect to the initial cell number.

We introduce a model based on a formalism of cell population dynamics accounting for both cell transition and division. Within such a formalism, linear models have been built up on the branching property, disregarding cellular interactions Kimmel and Axelrod (2015); Harris (1963), while nonlinear models

have accounted for interactions among different cell populations (e.g., typically, a feedback from differentiated cells onto precursor cells) either to ensure homeostasis, as in dynamical models for blood cells Getto and Marciniak-Czochra (2015); Stiehl and Marciniak-Czochra (2017); Pujo-Menjouet (2016), or to achieve a proper developmental sequence, as in dynamical models for neural cells Freret-Hodara et al. (2016). On our side, we are interested in assessing the duration of the activation process, and in ordering the events taking place during activation. A natural concept in probability theory to investigate these issues is the first passage time theory Darling and Siegert (1953); Van Kampen (1992), which aims to characterize the statistics of random events related to some particular outcomes. The analysis of first passage times are becoming more and more popular in mathematical biology Chou and D'Orsogna (2014); Castro et al. (2018), to quantify random times needed to reach a given final state, such as population extinction for instance. Typically, the parameters of cell dynamics models are calibrated using time series of cell counts sorted into different cell types Marr et al. (2012); Glauche et al. (2007). In contrast, in the case of early folliculogenesis, precursor and proliferative cell numbers are not available directly as a function of time, but only in relation with other morphological variables such as the oocyte and follicle diameters Braw-Tal and Yossefi (1997); Gougeon and Chainy (1987); Lundy et al. (1999); Meredith et al. (2000), so that we lack kinetic information. Yet, thanks to the discrete-time embedded Markov chain, we could apply here classical statistical tools like the maximum likelihood Wilkinson (2011), and related parameter identifiability concept Raue et al. (2009), by using the information on the state space alone.

Our model allows us to study the joint dynamics of the precursor cells F and proliferative cells C within a single follicle, whose populations are ruled by four types of possible cell events. Two cell events occur at the expense of the precursor cells, which are consumed during their transition : (i) $\mathcal{R}_1$ is the spontaneous transition of precursor cells into proliferative cells, whose rate $\alpha_1 F$ is linearly proportional to the number of precursor cells; (ii) $\mathcal{R}_2$ is the auto-amplified transition of precursor cells into proliferative cells, which occurs at rate $\beta_1 \frac{FC}{F+C}$. This event represents the feedback of proliferative cells onto the transition of the precursor cells. Two other cell events increase the proliferative cell population without affecting the precursor cell population: (i) $\mathcal{R}_3$ is an asymmetric division of precursor cells F (giving rise to one precursor cell and one proliferative cell), which occurs at rate $\alpha_2 F$; (ii) $\mathcal{R}_4$ is a symmetric division of the proliferative cells C (giving rise to two proliferative cells), which occurs at rate γC.
These four cell events are the building blocks of our main model $\mathcal{M}_{FC}$, which is summarized below :

$$
\begin{array}{lll}
 & \text{Cell events} & \text{Rate} \\
\mathcal{R}_1 : & (F,C) \to (F-1, C+1), & \alpha_1 F, \\
\mathcal{R}_2 : & (F,C) \to (F-1, C+1), & \beta_1 \frac{FC}{F+C}, \\
\mathcal{R}_3 : & (F,C) \to (F, C+1), & \alpha_2 F, \\
\mathcal{R}_4 : & (F,C) \to (F, C+1), & \gamma C\,.
\end{array}
\qquad (\mathcal{M}_{FC})
$$

Cell events $\mathcal{R}_1$ and $\mathcal{R}_4$ constitute the fundamental ingredients involved in the activation process. We also consider two additional cell events, $\mathcal{R}_3$ and $\mathcal{R}_4$, which are not only intended to enrich the model behavior, but are also substantiated by biological observations.
Cell event $\mathcal{R}_3$ considers that flattened (precursor) cells may divide before transition, which is consistent with experimental studies where KI67 staining (a marker of cell cycle progression) was detected in some flattened cells Da Silva-Buttkus et al. (2008). Since the number of flattened cells is non increasing, one can envisage the existence of self-renewing asymmetric divisions in flattened cells, giving birth to one proliferative cell (and keeping the precursor cell number unchanged).
Cell event $\mathcal{R}_2$ accounts for a possibly auto-amplified acceleration in cell shape transitions, which could result from the molecular mechanisms underlying follicle activation and establishing a dialog between the oocyte and somatic cells Monniaux (2016). In brief, the initiation signal (mTORC1) is first perceived by somatic cells Zhang et al. (2014), which then start stimulating the oocyte through specific signaling pathways (KIT-Ligand cytokine). In turn, once activated, the oocyte signals to the somatic cells through factors of the TGFβ family Knight and Glister (2006) (mainly GDF9 and BMP15). This molecular dialog settles a positive feedback loop, which can be represented by an auto-amplified transition rate. In sheep, there exist natural mutations affecting this molecular dialog (disruption of either the GDF9 or BMP15 ligand, or the receptor to BMP15). Introducing cell event $\mathcal{R}_2$ can help to investigate possible differences in the activation process in wild-type compared to mutant strains. More specifically, we have access to experimental cell numbers (courtesy of Ken McNatty) obtained either from a wild-type strain (Ile-de-France) or a mutant strain for BMP15R (Booroola), whose follicle development is known to be clearly different in the multi-layer stages Lundy et al. (1999), especially as far as cell dynamics. Whether cell dynamics is also affected during the mono-layer stage remains unclear Reader et al. (2012), which is an additional motivation for this work.

All the reactions rates (α_1, β_1, α_2 and γ) are non-negative. At initial time, there are only precursor cells, and the initial condition is chosen as a random positive integer variable, in consistency with the observed biological variability.

In the following, we will use different submodels derived from the full model $\mathcal{M}_{FC}$, by removing either one or several cell events (hence setting to zero the corresponding parameter values β_1, α_2 and/or γ). We will name these submodels by explicitly mentioning the remaining events. For instance, model $(\mathcal{R}_1, \mathcal{R}_3)$ consists only of the spontaneous cell transition event and asymmetric cell division ($\beta_1 = \gamma = 0$), while model $(\mathcal{R}_1, \mathcal{R}_4)$ is composed of the spontaneous cell transition event and asymmetric cell division ($\beta_1 = \alpha_2 = 0$).

Model $\mathcal{M}_{FC}$ can be mathematically formulated either with Ordinary Differential Equations (ODEs) or Continuous time Markov chain (CTMC) Gratie et al. (2013).
The stochastic description is especially appropriate when dealing with a small

number of cells. Even if the cell numbers in activating follicles are small, a deterministic formulation of model $\mathcal{M}_{FC}$ can still be convenient to get insight into the transient behavior of the cell populations and the parameter influence on the model outputs. Using the stochastic version of model $\mathcal{M}_{FC}$, we can illustrate the dynamics of both the precursor and proliferative cells (Figure 1). The C population grows as the F population decreases until extinction (top-left panel), and the proportion of proliferative cells $p_C := \frac{C}{F+C}$ increases monotonously from 0 to 1 (bottom-left panel). In the (C, F) phase plane (top-right panel), we can observe that the number of precursor cells remains constant (aligned red or black points on the horizontal line (k, F), $k \in \mathbb{N}$) whenever there is a division event ($\mathcal{R}_3$ or $\mathcal{R}_4$). In contrast, whenever there is a transition event ($\mathcal{R}_1$ or $\mathcal{R}_2$), the number of precursor cells decreases by one, as illustrated by the jump from the current line $((k, F), k \in \mathbb{N})$ to the lower one $((k, F-1),\ k \in \mathbb{N})$. Hence, in this simulation, we observe a sequence of transition and division events (which appear to be here mainly spontaneous transitions $\mathcal{R}_1$ and asymmetric divisions $\mathcal{R}_3$ due to the specific parameter choice). If we are only given the sequence of events in this plane, we cannot discriminate $\mathcal{R}_1$ from $\mathcal{R}_2$, neither $\mathcal{R}_3$ from $\mathcal{R}_4$. Note that, depending on the initial condition, some parts of the phase plane cannot be reached. The trajectories can also be observed in the (C, p_C) phase plane (bottom-right panel). In this case, the trajectories remain on the curves parameterized by $((k, \frac{k}{F+k}),\ k \in \mathbb{N})$ if a division event ($\mathcal{R}_3$ or $\mathcal{R}_4$) occurs, whereas they move to the upper curves parameterized by $((k, \frac{k}{F-1+k}),\ k \in \mathbb{N})$ whenever a transition event ($\mathcal{R}_1$ or $\mathcal{R}_2$) occurs.

The manuscript is organized as follows. After introducing the mathematical definitions in Section 2, we analyze both the deterministic and stochastic versions of model $\mathcal{M}_{FC}$ in Section 3. In subsection 3.1, we obtain the analytical solutions of the deterministic model, and explore the parameter influence on the model outputs. Subsection 3.2 deals with the Markov chain formulation of model $\mathcal{M}_{FC}$. In the linear case ($\beta_1 = 0$), we obtain analytical formulas for the mean extinction time. In the nonlinear case, we design a numerical scheme based on a rigorous Finite State Projection (see Munsky and Khammash (2006); Kuntz (2017)) and coupling techniques to assess the mean extinction time. In both cases, we study the sensitivity of the extinction time, as well as the cell number at extinction time, with respect to the parameter values. In section 4, using the embedded Markov chain, we calibrate the parameters of the different submodels and full model $\mathcal{M}_{FC}$ from our experimental, time-free datasets, and analyze the practical identifiability in each case. From data-fitting, we manage to retrieve hidden kinetic information and provide some biological interpretations of out results. We conclude in section 5.

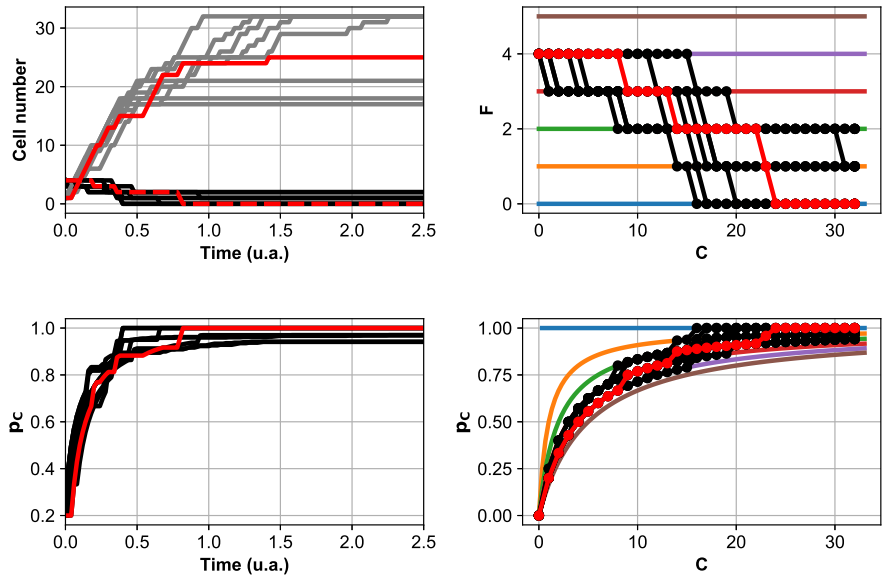

Fig. 1 Illustration of the dynamics generated by model $\mathcal{M}_{FC}$. The dynamics of the precursor and proliferative cells are computed using a Gillespie SSA algorithm Gillespie (2001) with the parameter values: $\alpha_1 = 1$, $\beta_1 = 0.01$, $\alpha_2 = 10$, $\gamma = 0.001$ and a deterministic initial condition $F(0) = 4$. In each panel, the black or gray lines represent 9 different trajectories of the process and the red line corresponds to one specific trajectory. Top-left panel: Number of precursor F (black lines) and proliferative C (gray lines) cells as a function of time. Bottom-left panel: Proportion p_C of proliferative cells as a function of time. Top-right panel: Number of precursor cells F as a function of the number proliferative cells C. Bottom-right panel: Proportion of proliferative cells p_C as a function of the number of proliferative cells C.

2 Model definition

Markov chain formulation On a probability space $(\Omega, \mathcal{F}, \mathbb{P})$, let the initial number of flattened cells F_0 be a positive integer random variable. The population of precursor cells F and proliferative cells C follows the Stochastic Differential Equation (SDE) below:

$$\begin{aligned} F_t &= F_0 - \mathcal{Y}_1\left(\int_0^t \alpha_1 F_s ds\right) - \mathcal{Y}_2\left(\int_0^t \beta_1 \frac{F_s C_s}{F_s + C_s} ds\right), \\ C_t &= \mathcal{Y}_1\left(\int_0^t \alpha_1 F_s ds\right) + \mathcal{Y}_2\left(\int_0^t \beta_1 \frac{F_s C_s}{F_s + C_s} ds\right) \\ &\quad + \mathcal{Y}_3\left(\int_0^t \alpha_2 F_s ds\right) + \mathcal{Y}_4\left(\int_0^t \gamma C_s ds\right). \end{aligned} \quad (1)$$

where $\mathcal{Y}_i$, for all $i = 1, 2, 3, 4$, are mutually independent standard Poisson processes. $X = (X_t)_{t \geq 0}$, with $X_t := (F_t, C_t)$ for all $t \geq 0$, denotes the solu-

tion of (1). $(\mathcal{F}_t)_{t\geq 0}$ denotes the canonical filtration generated by the process X.

We can also see X as a continuous-time Markov chain with countable state space $\mathcal{S} := \mathbb{N}^2\backslash\{(0,0)\}$ and transition matrix $Q := (q(x,y))_{x,y\in\mathcal{S}}$, with for all $(f,c) \in \mathcal{S}$,

$$\begin{aligned} q\left((f,c),(f-1,c+1)\right) = &\quad \alpha_1 f + \beta_1 \frac{fc}{f+c}, \\ q\left((f,c),(f,c+1)\right) &= \alpha_2 f + \gamma c. \end{aligned}$$

We recall that Q is linked to the infinitesimal generator $\mathcal{L}$ by the Dynkin's formula (Theorem 2.2, p.380, Brémaud (2013)):

$$\mathcal{L}g(x) = \sum_{y\in\mathcal{S}, y\neq x} q(y,x)g(y) - q(x)g(x), \text{ where } q(x) = \sum_{y\in\mathcal{S}, y\neq x} q(x,y).$$

Thus, the infinitesimal generator $\mathcal{L}$ of X is given by

$$\begin{aligned} \mathcal{L}g(f,c) = (\alpha_1 f + \beta_1 \frac{fc}{f+c}) \left[g(f-1,c+1) - g(f,c)\right] \\ + (\alpha_2 f + \gamma c) \left[g(f,c+1) - g(f,c)\right], \end{aligned} \quad (2)$$

for all g bounded functions and for all $(f,c) \in \mathcal{S}$.

In the whole study, we will need the following hypotheses:

Hypothesis 1 *The spontaneous activation rate α_1 is positive.*

Hypothesis 2 *The initial condition F_0 is L_2-integrable.*

For specific results, we will also need an additional hypothesis:

Hypothesis 3 *The spontaneous activation rate α_1 is strictly greater than the proliferation rate γ: $\alpha_1 > \gamma$.*

With Hypothesis 2, we apply Theorem 1.22 of Anderson and Kurtz (2015) (p.12-13) and deduce that the process M_t^g defined as

$$M_t^g := g(X_t) - g(X_0) - \int_0^t \mathcal{L}g(X_s)ds \quad (3)$$

is a $\mathcal{F}_t$-martingale, for all $t \geq 0$.

Note that the F process is a non-negative decreasing process. To study the hitting time of the state $F = 0$, we introduce the following definition

Definition 1 Let τ^{F_0} be the extinction time of the precursor cell population F

$$\tau^{F_0} := \inf\{t \geq 0; \quad F_t = 0 | F_0\}. \quad (4)$$

The number of proliferative cells C at $t = \tau^{F_0}$ is $C_{\tau^{F_0}}$.

Mean-field formulation To get some insight into the model, we describe the mean-field version of the model $\mathcal{M}_{FC}$, given by the set of ODE below:

$$\begin{cases} \frac{d}{dt}f(t) = -\alpha_1 f(t) - \beta_1 f(t)\frac{c(t)}{f(t)+c(t)}, \\ \frac{d}{dt}c(t) = (\alpha_1+\alpha_2)f(t) + \beta_1 f(t)\frac{c(t)}{f(t)+c(t)} + \gamma c(t), \end{cases} \tag{5}$$

with the initial condition $(f(0), c(0)) = (f_0, 0)$, with $f_0 \in \mathbb{R}_+$.

3 Model analysis

In this section we analyze the cell dynamics of the precursor and proliferative cells both for the deterministic and stochastic versions of model $\mathcal{M}_{FC}$. We start by solving analytically the deterministic formulation, and investigate the effect of each parameter on the model outputs. Then, we study the mean extinction time of the precursor cell population and the number of proliferative cells at that time.

3.1 Analysis of the deterministic model

From the ODE sytem (5), we deduce the change in the proliferative cell proportion $p_C(t) := \frac{c(t)}{f(t)+c(t)}$:

$$\begin{aligned} \frac{d}{dt}p_C(t) &= \alpha_1 + \alpha_2 - (\alpha_1 + 2\alpha_2 - \beta_1 - \gamma)p_C(t) + (\alpha_2 - \beta_1 - \gamma)p_C(t)^2 \\ &= (\alpha_2 - \beta_1 - \gamma)(p_C(t) - 1)(p_C(t) - \frac{\alpha_1+\alpha_2}{\alpha_2 - \beta_1 - \gamma}). \end{aligned} \tag{6}$$

From ODEs (5) and (6), using the classical method of separation of variables, we can compute the analytical expressions for the proliferative cell proportion $p_C(t)$, proliferative cell number $c(t)$ and precursor cell number $f(t)$:

Proposition 1 *The solution of the ODE system* (5) *is, for all* $t \geq 0$,

$$\begin{aligned} f(t) &= f_0 \exp\left(-\alpha_1 t - \beta_1 \int_0^t p_C(s)ds\right), \\ c(t) &= f_0 \left(\exp\left(\alpha_2 t + (\gamma - \alpha_2)\int_0^t p_C(s)ds\right) - \exp\left(-\alpha_1 t - \beta_1 \int_0^t p_C(s)ds\right)\right). \end{aligned}$$

In addition, the solution of ODE (6) *is*

$$p_C(t) = \frac{1 - \exp\left(-(\alpha_1+\beta_1+\gamma)t\right)}{1 - \frac{\alpha_2-\beta_1-\gamma}{\alpha_1+\alpha_2}\exp\left(-(\alpha_1+\beta_1+\gamma)t\right)}. \tag{7}$$

Remark 1 *The total cell number verifies*

$$n(t) := f(t) + c(t) = f_0 \exp\left(\alpha_2 t + (\gamma - \alpha_2)\int_0^t p_C(s)ds\right).$$

As the proliferative cell proportion p_C converges to 1, the total cell number grows exponentially, first at rate α_2 and then at rate γ.

We illustrate the changes in the state variables along time on Figure 2, for different parameter configurations corresponding to different submodels. The transition kinetics of the precursor cells can either follow an exponential decay when β_1 is zero (or much smaller than α_1), or a sharper transition when β_1 is larger than α_1, with a sigmoid-like shape and an inflexion point (top-left panel). The growth kinetics of the proliferative cells can be characterized by three types of behavior (top-middle and top-right panels):

- a saturated growth with steadily decreasing speed with submodels $(\mathcal{R}_1)$ and $(\mathcal{R}_1, \mathcal{R}_3)$,
- an exponential growth as long as $\gamma > 0$ with submodel $(\mathcal{R}_1, \mathcal{R}_4)$,
- a logistic growth when the feedback term is strong enough (submodel $(\mathcal{R}_1, \mathcal{R}_2)$).

The growth kinetics of the total cell number behaves accordingly (bottom-right panel), with three possible patterns: exponential growth, saturated growth for submodel $(\mathcal{R}_1)$, and steadiness for submodel $(\mathcal{R}_1, \mathcal{R}_2)$. Finally, the proportion p_C (bottom-left panel) may either increase in a saturated manner (with steadily decreasing speed, submodels $(\mathcal{R}_1)$ and $(\mathcal{R}_1, \mathcal{R}_3)$), or in a sigmoid-like manner (with a change in the acceleration sign) if β_1 or γ are high enough. The inflexion point of $t \mapsto p_C(t)$ can be computed from the analytical solution (7):

$$\bar{p}_C = \frac{\alpha_1 + 2\alpha_2 - (\beta_1 + \gamma)}{2\alpha_2 - 2(\beta_1 + \gamma)}.$$

Note that according to the observed variables, the submodels cannot be distinguished from one another, or, alternatively, different parameter values (within a same submodel) may lead to identical outputs. Indeed, the changes in the precursor cell population are independent of parameters α_2, γ, and, more strikingly, parameters β_1 and γ cannot be separated in the analytical solution (7), leading to the same kinetic patterns as long as the combination $\gamma + \beta_1$ remains unchanged.

From Proposition 1, we deduce that p_C is a strictly increasing function, hence we can invert the p_C function and deduce that $\forall t \in \mathbb{R}_+, \exists! p \in [0, 1)$, such that

$$t(p) = p_C^{-1}(p) = \frac{-1}{(\alpha_1 + \beta_1 + \gamma)} \ln\left(\frac{1-p}{1 - p\frac{\alpha_2 - \beta_1 - \gamma}{\alpha_1 + \alpha_2}}\right). \tag{8}$$

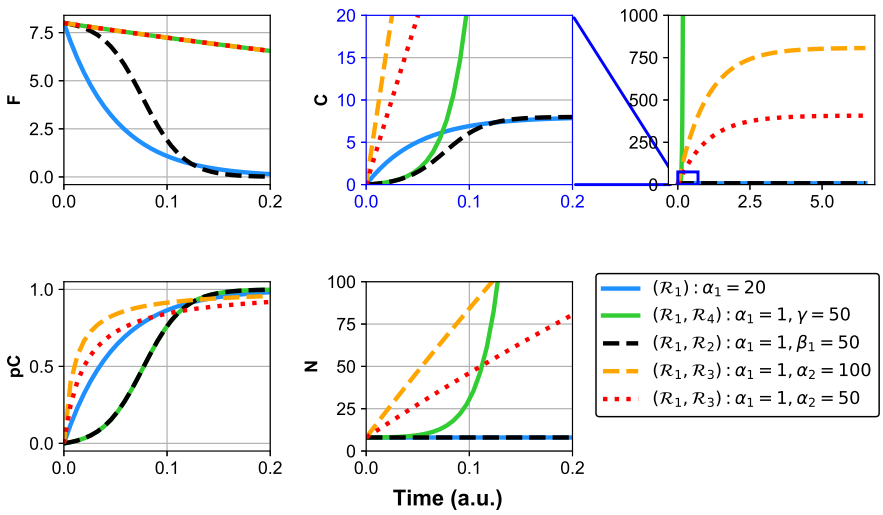

Fig. 2 Parameter influence on the outputs of the deterministic model. From ODEs (5) and (6), we compute numerically (using the Python solver odeint from the package scipy.integrate), for different parameter values, the different model outputs as a function of time. Top-left panel: precursor cell number $f(t)$. Top-middle panel: proliferative cell number $c(t)$, with a zoom insert in the top-right panel. Bottom-left panel: proliferative cell proportion $p_C(t)$. Bottom-middle panel: total cell number $n(t)$. The legend insert specifies the (non-zero) parameter values corresponding to each submodel and the color code. Blue line: submodel $(\mathcal{R}_1)$ with $\alpha_1 = 20$; green line: submodel $(\mathcal{R}_1, \mathcal{R}_4)$ with $\alpha_1 = 1$ and $\gamma = 50$; black dashed line: submodel $(\mathcal{R}_1, \mathcal{R}_2)$ with $\alpha_1 = 1$ and $\beta_1 = 50$; orange dashed line: submodel $(\mathcal{R}_1, \mathcal{R}_3)$ with $\alpha_1 = 1$ and $\alpha_2 = 100$; red dotted line: submodel $(\mathcal{R}_1, \mathcal{R}_3)$ with $\alpha_1 = 1$ and $\alpha_2 = 50$. In each case, the initial number of precursor cells is fixed to $f_0 = 8$.

3.2 Analysis of the extinction of the precursor cell population

To simplify the proofs, we will consider in the following that the initial condition is a deterministic value $f_0 \in \mathbb{N}^*$. All the proofs can be generalized to the random F_0 case by conditioning by the law of F_0.

3.2.1 Analytical expressions in the linear case

When β_1 is zero, the process X is linear, and we can compute the law of the extinction time. In the case when, in addition, either α_2 or γ is zero, or both are zero, the mean number of proliferative cells at extinction time can also be computed.
In this subsection we will write $X_t^L = (F_t^L, C_t^L)$ the solution of the SDE (1) when $\beta_1 = 0$ and $\tau_L^{f_0}$ the associated extinction time of the population F_t^L:

$$\tau_L^{f_0} := \inf\{t; \quad F_t^L = 0 | f_0\}\,. \tag{9}$$

Note that the F^L process is independent of the C^L process. The jumping times T_k of F^L, for all $k \in [\![0, f_0 - 1]\!]$, are given by

$$T_{k+1} := T_k + \mathcal{E}\left(\alpha_1(f_0 - k)\right), \tag{10}$$

with $T_0 = 0$ by convention. Note that $T_{f_0} = \tau_L^{f_0}$.

Proposition 2 (F_t^L and $\tau_L^{f_0}$ laws) *Under Hypothesis 1 and for all $t \geq 0$, $F_t^L | F_0 = f_0$ follows a binomial law with parameters $(n, p) = (f_0, e^{-\alpha_1 t})$, and the extinction time $\tau_L^{f_0}$, defined by formula (9), follows a generalized Erlang law (or hypo-exponential law) of density:*

$$f_{\tau_L^{f_0}}(t) = \alpha_1 f_0 e^{-\alpha_1 t}(1 - e^{-\alpha_1 t})^{f_0 - 1} \mathbb{1}_{[0,+\infty[}(t), \tag{11}$$

such that $\mathbb{E}\left[\tau_L^{f_0}\right] = \dfrac{1}{\alpha_1} \displaystyle\sum_{k=1}^{f_0} \frac{1}{k}$.

Proof Let $t \geq 0$ and $f \in [\![0, f_0]\!]$. Since F_t is autonomous and is a pure death process, we can directly write the following forward Kolmogorov equation: for all $f \in [\![0, f_0]\!]$,

$$\frac{d}{dt}\mathbb{P}\left[F_t^L = f | F_0 = f_0\right] = \\ \alpha_1(f+1)\mathbb{P}\left[F_t^L = f+1 | F_0 = f_0\right] - \alpha_1 f \mathbb{P}\left[F_t^L = f | F_0 = f_0\right]. \tag{12}$$

Solving by recurrence (12), we deduce that, for all $f \in [\![0, f_0]\!]$,

$$\mathbb{P}\left[F_t^L = f | F_0 = f_0\right] = \binom{f_0}{f} (e^{-\alpha_1 t})^f (1 - e^{-\alpha_1 t})^{f_0 - f}.$$

Note that $\mathbb{P}\left[F_t = 0 | F_0 = f_0\right] = (1 - e^{-\alpha_1 t})^{f_0}$ which converges to 1 when t goes to infinity. Hence, the process F^L extincts almost surely (a.s.) when t goes to infinity, hence $\tau_L^{f_0} < \infty$. Before computing the law of $\tau_L^{f_0}$, we can directly obtain its mean using the recursive expression (10):

$$\mathbb{E}\left[\tau_L^{f_0}\right] = \sum_{k=0}^{f_0 - 1} \mathbb{E}\left[T_{k+1} - T_k\right] = \sum_{k=0}^{f_0 - 1} \mathbb{E}\left[\mathcal{E}\left(\alpha_1(f_0 - k)\right)\right] = \frac{1}{\alpha_1} \sum_{k=1}^{f_0} \frac{1}{k}.$$

Then, using the same recursive expression (10), we deduce that $\tau_L^{f_0} (= T_{f_0})$ follows a generalized Erlang law whose density function is:

$$f_{\tau_L^{f_0}}(t) = \mathbb{1}_{t \geq 0} \sum_{i=0}^{f_0 - 1} \prod_{j \neq i, j=0}^{f_0 - 1} \frac{f_0 - j}{i - j} \alpha_1 (f_0 - i) e^{-\alpha_1 (f_0 - i) t}. \tag{13}$$

Due to the specific form of the exponential rate in Eq. (13), we can simplify it further. As $\prod_{j\neq i, j=0}^{f_0-1}(f_0-j) = \frac{f_0!}{f_0-i}$ and

$$\begin{aligned}\prod_{j\neq i, j=0}^{f_0-1}(i-j) &= \prod_{j=0}^{i-1}(i-j) \times \prod_{j=i+1}^{f_0-1}(i-j)\\ &= i!(-1)^{f_0-1-i}\prod_{j=1}^{f_0-1-i} j = (-1)^{f_0-1-i} i!(f_0-1-i)!,\end{aligned}$$

we deduce

$$\begin{aligned}f_{\tau_L^{f_0}}(t) =& \alpha_1 \mathbb{1}_{t\geq 0}\sum_{i=0}^{f_0-1}\frac{f_0!}{i!(f_0-1-i)!}(-1)^{f_0-1-i}e^{-\alpha_1(f_0-i)t}\\ =& \alpha_1 f_0 e^{-\alpha_1 t}\mathbb{1}_{t\geq 0}\sum_{i=0}^{f_0-1}\binom{f_0-1}{i}(-e^{-\alpha_1 t})^{f_0-i-1}\\ =& \alpha_1 f_0 e^{-\alpha_1 t}(1-e^{-\alpha_1 t})^{f_0-1}\mathbb{1}_{t\geq 0}.\end{aligned}$$

□

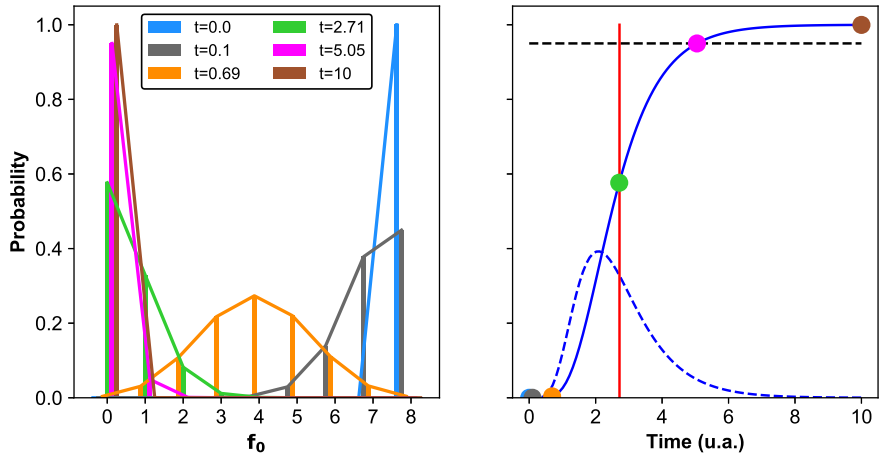

Fig. 3 Illustration of Proposition 2. Left-panel: Distribution of the random variable F_t^L (binomial law) given the initial value $F_0 = 8$. Each colored bar plot/line corresponds to a different time (t=0,0.1,0.69,2.71,5.05, 10), see color code in the legend insert. Right-panel: Extinction time of the precursor cells. The blue solid line is the cumulative distribution function of the extinction time $\tau_L^{f_0}$, while the blue dashed line is the probability density function. The vertical red line indicates the mean extinction time value. The horizontal black dashed line indicates the 95% confidence level. The colored points indicate the time points corresponding to the legend insert. In both panels, $\alpha_1 = 1$.

Figure 3 illustrates both the precursor cell distribution at different times (left panel) and the extinction time distribution of precursor cells (right panel) in the linear model $(\mathcal{R}_1, \mathcal{R}_3, \mathcal{R}_4)$. Thanks to the analytical solutions, one can easily compute a confidence interval for the extinction time. For instance, we compute the time $t = t_{0.95}$ for which extinction has occurred with probability 0.95,

$$\mathbb{P}\left[F_{t_{0.95}} = 0 | F_0 = f_0\right] = 1 - e^{-\alpha_1 f_0 t_{0.95}} \geq 0.95 \Rightarrow t_{0.95} \geq -\frac{\ln(0.05)}{\alpha_1 f_0} \approx \frac{3}{\alpha_1 f_0}.$$

We now study the mean number of proliferative cells at the extinction time. We define the stochastic processes $C^{k,j}$, for $(k,j) \in \mathbb{N} \times \mathbb{N}$, as independent and identically distributed Yule processes. We recall that the Yule process can be seen as the solution of

$$C_t^{0,0} = 1 + \mathcal{Y}\left(\gamma \int_0^t C_s^{0,0} ds\right),$$

where $\mathcal{Y}$ is a Poisson process.
Since the process C_t^L is linear, hence is a branching process, it can be written as the sum of independent and identically distributed elementary processes $C^{k,j}$ (cell lineages, see Figure 4): for all $t \geq 0$,

$$C_t^L = \underbrace{\sum_{k=1}^{F_0} C_{t-T_k^0}^{k,0} \mathbb{1}_{t \geq T_k^0}}_{\text{cell lineages generated by cell event } \mathcal{R}_1} + \underbrace{\sum_{k=0}^{F_0-1} \sum_{j=1}^{N_k(t)} C_{t-T_k^j}^{k,j} \mathbb{1}_{t \geq T_k^j}}_{\text{cell lineages generated by cell event } \mathcal{R}_3}, \tag{14}$$

where we define, for all $k \in [\![1, f_0]\!]$,

- $T_k^0 := T_k$ (with T_k given by equation (10)), the k-th jumping time of the cell event $\mathcal{R}_1$ of $\mathcal{M}_{FC}$.
- $N_k(t)$, the number of occurrences of cell event $\mathcal{R}_3$ between T_k and T_{k+1}, for $t \geq T_k$. Note that

$$N_k(t) = \mathcal{Y}_3\left(\alpha_2 \int_0^{t \wedge T_{k+1}} F_s^L ds\right) - \mathcal{Y}_3\left(\alpha_2 \int_0^{T_k} F_s^L ds\right). \tag{15}$$

- for all $j \in [\![1, N_k(t)]\!]$,

$$T_k^j := T_k^{j-1} + \mathcal{E}\left(\alpha_2 (f_0 - k)\right), \tag{16}$$

  the j-th jumping time of the cell event $\mathcal{R}_3$ occurring between the two random times T_k and T_{k+1}.

According to Proposition 2, $\tau_L^{f_0}$ is a.s. finite. To take the expectation of C_t^L at time $t = \tau_L^{f_0}$, we check that $\mathbb{E}\left[C_{\tau_L^{f_0} - T_k^j}^{k,j}\right] < \infty$, for all k and j. For all $t \geq 0$,

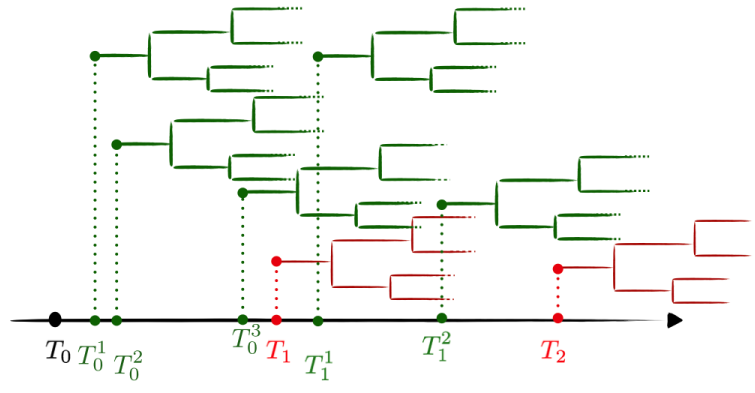

Fig. 4 Jumping times and cell lineages. Each cell lineage represents schematically the random process $C^{k,j}$, arising either from the cell event $\mathcal{R}_1$ (green trees) or $\mathcal{R}_2$ (red trees), for the linear version of model $\mathcal{M}_{FC}$ (submodel $(\mathcal{R}_1, \mathcal{R}_3, \mathcal{R}_4)$). For all $k \in [\![0, f_0]\!]$, the random times T_k are defined by equation (10) and, for all $j \in [\![1, N_k(t)]\!]$ where $N_k(t)$ is given by equation (15), the random times T_k^j are defined by equation (16). The times of the subsequent symmetric division events following the T_k^j and T_k times are represented at arbitrary time points.

$C_t^{k,j}$ is L_1-integrable (as a Yule process) with $\mathbb{E}\left[C_t^{k,j}\right] = e^{\gamma t}$. Note that

$$I := \int_0^{+\infty} e^{\gamma t} f_{\tau_L^{f_0}}(t)dt = \alpha_1 f_0 \int_0^t e^{(\gamma-\alpha_1)t}(1-e^{-\alpha_1 t})^{f_0-1}dt$$
$$= \alpha_1 F_0 \sum_{i=0}^{f_0-1} \binom{f_0-1}{i} \int_0^{+\infty} e^{(\gamma-\alpha_1(i+1))t}dt.$$

If Hypothesis 3 holds, $I < \infty$ and, since $C^{k,j}$ is a positive increasing process, we deduce:

$$\mathbb{E}\left[C^{k,j}_{\tau_L^{f_0}-T_k^j}\right] \leq \mathbb{E}\left[C^{k,j}_{\tau_L^{f_0}}\right] = I < \infty.$$

Then, taking the expectation of (14) at time $t = \tau_L^{f_0}$, we obtain:

$$\mathbb{E}\left[C^L_{\tau_L^{f_0}}\right] = \sum_{k=1}^{f_0} \mathbb{E}\left[C^{k,0}_{\tau_L^{f_0}-T_k^0}\right] + \sum_{k=0}^{f_0-1} \mathbb{E}\left[\sum_{j=1}^{N_k(\tau_L^{f_0})} C^{k,j}_{\tau_L^{f_0}-T_k^j}\right]. \tag{17}$$

In some cases, the latter formulas can be used to obtain the first moment of $C^L_{\tau_L^{f_0}}$.

Proposition 3 (First moment of $C^L_{\tau_L^{f_0}}$)

1. *Under Hypothesis 1, and supposing that γ is zero,*

$$\mathbb{E}\left[C^L_{\tau_L^{f_0}}\right] = f_0(1+\frac{\alpha_2}{\alpha_1}).$$

2. Under Hypotheses 1 and 3, and supposing that α_2 is zero,

$$\mathbb{E}\left[C^L_{\tau_L^{f_0}}\right] = 1 + \alpha_1 \sum_{k=1}^{f_0-1} (f_0-k) \sum_{i=0}^{f_0-k-1} \binom{f_0-k-1}{i} \frac{(-1)^{i+1}}{\gamma - \alpha_1(i+1)}.$$

Proof When γ is zero, then for all $t \geq 0$, for all $k \in [\![1, f_0]\!]$ and for all $j \in [\![1, N_k(\tau_L^{f_0})]\!]$, $C_t^{k,j} = 1$. We deduce directly from Eq. (17) that

$$\mathbb{E}\left[C^L_{\tau_L^{f_0}}\right] = f_0 + \sum_{k=0}^{f_0-1} \mathbb{E}\left[N_k(\tau_L^{f_0})\right]. \tag{18}$$

From Eq. (15), we have

$$\begin{aligned}\mathbb{E}\left[N_k(\tau_L^{f_0})\right] &= \mathbb{E}\left[\mathcal{Y}_3\left(\alpha_2 \int_0^{T_{k+1}} F_s^L ds\right) - \mathcal{Y}_3\left(\alpha_2 \int_0^{T_k} F_s^L ds\right)\right] \\ &= \mathbb{E}\left[\mathcal{Y}_3\left(\alpha_2 \int_{T_k}^{T_{k+1}} F_s^L ds\right)\right] = \mathbb{E}\left[\alpha_2 \int_{T_k}^{T_{k+1}} F_s^L ds\right],\end{aligned}$$

by Poisson process property. Since for all $t \in [T_k, T_{k+1})$, $F_t^L = f_0 - k$, we deduce $\mathbb{E}\left[N_k(\tau_L^{f_0})\right] = \mathbb{E}\left[\alpha_2(f_0-k)(T_{k+1}-T_k)\right]$. Using (10), we deduce that $\mathbb{E}\left[N_k(\tau_L^{f_0})\right] = \frac{\alpha_2(f_0-k)}{\alpha_1(f_0-k)} = \frac{\alpha_2}{\alpha_1}$ and conclude with (18).

When α_2 is zero, $N_k(t)$ is null for all $t \geq 0$, hence we deduce directly from (17) that

$$\mathbb{E}\left[C^L_{\tau_L^{f_0}}\right] = \sum_{k=1}^{f_0} \mathbb{E}\left[C^{k,0}_{\tau_L^{f_0}-T_k}\right]. \tag{19}$$

Since $T_{f_0} = \tau_L^{f_0}$, we have $C^{f_0,0}_{\tau_L^{f_0}-T_{f_0}} = 1$. Let $k \in [\![1, f_0-1]\!]$. Since $\tau_L^{f_0} - T_k \overset{(law)}{=} \sum_{i=k+1}^{f_0} \mathcal{E}\left(\alpha_1(f_0-i+1)\right) \overset{(law)}{=} \sum_{i=1}^{f_0-k} \mathcal{E}\left(\alpha_1 i\right)$, using Proposition 2, we deduce that the density function of $\tau_L^{f_0} - T_k$ is

$$f_{\tau_L^{f_0}-T_k}(t) = \alpha_1(f_0-k)e^{-\alpha_1 t}(1-e^{-\alpha_1 t})^{f_0-k-1}\mathbb{1}_{t\geq 0}.$$

Then, conditioning $C^{k,0}_{\tau_L^{f_0}-T_k}$ by the law of $\tau_L^{f_0} - T_k$, we deduce first

$$\mathbb{E}\left[C^{k,0}_{\tau_L^{f_0}-T_k}\right] = \int_0^{+\infty} \mathbb{E}\left[C_t^{k,0}\right] f_{\tau_L^{f_0}-T_k}(t)dt,$$

then, since $\mathbb{E}\left[C_t^{k,0}\right] = e^{\gamma t}$,

$$\begin{aligned}\mathbb{E}\left[C^{k,0}_{\tau_L^{f_0}-T_k}\right] &= \alpha_1(f_0-k)\int_0^{+\infty} e^{(\gamma-\alpha_1)t}(1-e^{-\alpha_1 t})^{f_0-k-1}dt \\ &= \alpha_1(f_0-k)\sum_{i=0}^{f_0-k-1}\binom{f_0-k-1}{i}\int_0^{+\infty}(-1)^i e^{(\gamma-\alpha_1(i+1))t}dt \\ &= \alpha_1(f_0-k)\sum_{i=0}^{f_0-k-1}\binom{f_0-k-1}{i}\frac{(-1)^{i+1}}{\gamma-\alpha_1(i+1)},\end{aligned}$$

which ends the proof using (19).

□

The influence of each parameter on the mean number of proliferative cells at the extinction time, $\mathbb{E}\left[C^L_{\tau_L^{f_0}}\right]$, for the linear model $(\mathcal{R}_1, \mathcal{R}_3, \mathcal{R}_4)$, are illustrated in Figure 5. We observe that $C^L_{\tau_L^{f_0}}$ grows without bound as the symmetric division rate γ approaches α_1 (submodel $(\mathcal{R}_1, \mathcal{R}_4)$), while it grows linearly as a function of the asymmetric division rate α_2 (submodel $(\mathcal{R}_1, \mathcal{R}_3)$). Both behaviors are consistent with the deterministic results (Figure 2).

Remark 2 *In the case when both $\alpha_2 > 0$ and $\gamma > 0$, a simple analytical formula cannot be obtained for the first moment of $C^L_{\tau_L^{f_0}}$ since it is tricky to deal with expectation in the second term of relation* (14).

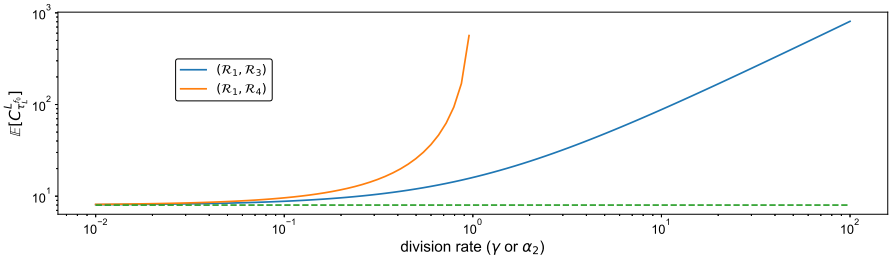

Fig. 5 Illustration of Proposition 3. Mean number of proliferative cells at the extinction time, $\mathbb{E}\left[C^L_{\tau_L^{f_0}}\right]$ for different parameter values. Orange line: $\mathbb{E}\left[C^L_{\tau_L^{f_0}}\right]$ with respect to γ in submodel $(\mathcal{R}_1, \mathcal{R}_4)$ ($\alpha_2 = 0$). Blue line: $\mathbb{E}\left[C^L_{\tau_L^{f_0}}\right]$ with respect to α_2 in submodel $(\mathcal{R}_1, \mathcal{R}_3)$ ($\gamma = 0$). Green dashed line: both α_2 and γ are zero, hence $\mathbb{E}\left[C^L_{\tau_L^{f_0}}\right] = f_0 = 8$. In all cases, $\alpha_1 = 1$.

3.2.2 Upper bound of the stochastic model – Eq. (1)

In the general case, we cannot obtain analytical expressions for the extinction time, and we will rather use numerical simulations. To control the numerical error, we need a tractable upper bound of the stochastic model introduced in Eq. (1), which is obtained in this subsection.

Let $\mathcal{L}_F^{sup}$ and $\mathcal{L}_C^{sup}$ be the following operators:

$$\mathcal{L}_F^{sup}\phi(f) = \alpha_1 f\left[\phi(f-1) - \phi(f)\right],$$
$$\mathcal{L}_C^{sup}\phi(c) = \left[(\alpha_1 + \beta_1 + \alpha_2)f_0 + \gamma c\right]\left[\phi(c+1) - \phi(c)\right].$$

for all ϕ bounded functions, for all $f, c \in \mathbb{N}$.

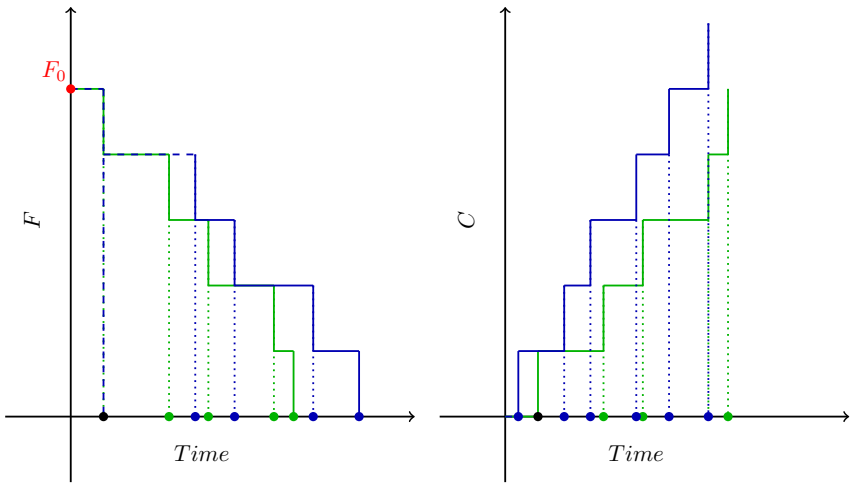

Fig. 6 Schematic trajectories of the coupled processes (F^{sup}, C^{sup}) and $X = (F, C)$. Left panel: number of precursor cells F (in green) and upper bound F^{sup} (in blue). Right panel: number of proliferative cells C (in green) and upper bound C^{sup} (in blue).

Proposition 4 (Coupling) *For the X process, there exist processes F^{sup} and C^{sup} of generator $\mathcal{L}_F^{sup}$ and $\mathcal{L}_C^{sup}$, respectively, such that for all $t \in \mathbb{R}_+$, $F_t^{sup} \geq F_t$ and $C_t^{sup} \geq C_t$ a.s.*

Figure 6 illustrates (schematically) the upper bound (F^{sup}, C^{sup}) of the process $X = (F, C)$ solution of model $\mathcal{M}_{FC}$. This upper bound is obtained from an appropriate coupling of both processes, which may or may not jump together, and which are such that when $F^{sup} = F$ (resp. $C^{sup} = C$), the process F^{sup} (resp. C^{sup}) jumps after (resp. before) the process F (resp. C), which ensures keeping the order $F^{sup} \geq F$ (resp. $C^{sup} \geq C$). The coupling is explicit

in the proof of Proposition 4. We define F^{sup} and C^{sup} as the solutions of the SDEs:

$$F_t^{sup} = f_0 - \mathcal{Y}_1\left(\alpha_1 \int_0^t F_s^{sup} ds\right),$$
$$C_t^{sup} = \mathcal{Y}_1\left(\alpha_1 f_0 t\right) + \mathcal{Y}_2\left(\beta_1 f_0 t\right) + \mathcal{Y}_3\left(\alpha_2 f_0 t\right) + \mathcal{Y}_4\left(\gamma \int_0^t C_s^{sup} ds\right), \quad (20)$$

where the Poisson processes $(\mathcal{Y}_i)_{i=1..4}$ are the same as those in Eq. (1). By additivity of independent Poisson processes, we deduce that the infinitesimal generator of F^{sup} and C^{sup} are $\mathcal{L}_F^{sup}$ and $\mathcal{L}_C^{sup}$, respectively.

Remark 1 The C^{sup} process is linear, as the C^L process introduced in subsection 3.2.1. It turns out that the C^{sup} process yields a much more tractable analytical expression to control the mean number of proliferative cells at the extinction time.

To prove the upper bound for the C process, we first start by a lemma.

Lemma 1 *For $i = 1, 2, 3$, let $(U_k^i)_{k\geq 0}$ be the sequences of jumping times associated with the counting processes*

$$t \mapsto \mathcal{Y}_1\left(\int_0^t \alpha_1 F_s ds\right), \quad t \mapsto \mathcal{Y}_2\left(\int_0^t \beta_1 \frac{F_s C_s}{F_s + C_s} ds\right),$$
$$\text{and} \quad t \mapsto \mathcal{Y}_3\left(\int_0^t \alpha_2 F_s ds\right)$$

respectively, and, for $i = 1, 2, 3$, let $(V_k^i)_{k\geq 0}$ be the sequences of jumping times associated with the counting processes

$$t \mapsto \mathcal{Y}_1\left(\alpha_1 f_0 t\right), t \mapsto \mathcal{Y}_2\left(\beta_1 f_0 t\right), \text{ and } t \mapsto \mathcal{Y}_3\left(\alpha_2 f_0 t\right)$$

respectively. We also define the process $Z_t^U := \sum_{i=1}^{3} \sum_{k\geq 1} \mathbb{1}_{\{U_k^i \leq t\}}$ and the process $Z_t^V := \sum_{i=1}^{3} \sum_{k\geq 1} \mathbb{1}_{\{V_k^i \leq t\}}$.
For all $t \geq 0$,

$$Z_t^U \leq Z_t^V, \text{ a.s.} \quad (21)$$

Proof (Proof of Lemma 1) By definition of a standard Poisson process, there exists a sequence of jumping times $(S_k^i)_{k\geq 0}$ for each $i = 1, 2, 3$ such that

$$\mathcal{Y}_i(t) = \sum_{k\geq 1} \mathbb{1}_{\{S_k^i \leq t\}}.$$

By definition of $(S_k^i)_{k\geq 0}$ and $(U_k^i)_{k\geq 0}$, for each $i = 1, 2, 3$ and for all $k \geq 0$, we have

$$\int_{U_k^1}^{U_{k+1}^1} \alpha_1 F_s ds = S_{k+1}^1 - S_k^1, \quad (22)$$

$$\int_{U_k^2}^{U_{k+1}^2} \beta_1 \frac{F_s C_s}{F_s + C_s} ds = S_{k+1}^2 - S_k^2, \tag{23}$$

$$\int_{U_k^3}^{U_{k+1}^3} \alpha_2 F_s ds = S_{k+1}^3 - S_k^3, \tag{24}$$

Also, by definition of $(S_k^i)_{k\geq 0}$ and $(V_k^i)_{k\geq 0}$, for each $i = 1, 2, 3$ and for all $k \geq 0$, we have

$$V_{k+1}^1 - V_k^1 = \frac{S_{k+1}^1 - S_k^1}{\alpha_1 f_0}, \quad V_{k+1}^2 - V_k^2 = \frac{S_{k+1}^2 - S_k^2}{\beta_1 f_0} \text{ and } V_{k+1}^3 - V_k^3 = \frac{S_{k+1}^3 - S_k^3}{\alpha_2 f_0}. \tag{25}$$

From (22)-(24), we obtain

$$S_{k+1}^1 - S_k^1 \leq \alpha_1 f_0 (U_{k+1}^1 - U_k^1),\ S_{k+1}^2 - S_k^2 \leq \beta_1 f_0 (U_{k+1}^2 - U_k^2) \text{ and } S_{k+1}^3 - S_k^3 \leq \alpha_2 f_0 (U_{k+1}^3 - U_k^3). \tag{26}$$

Combining (25) and (26) , we conclude that for each $i = 1, 2, 3$

$$V_{k+1}^i - V_k^i \leq U_{k+1}^i - U_k^i. \tag{27}$$

We obtain that, for all $t \geq 0$, $Z_t^U \leq Z_t^V$ a.s. , by counting process definition.

□

We can now proceed to the proof of Proposition 4.

Proof (Proof of Proposition 4) The C and $C^{\sup}$ processes start from the same state: $C_0 = C_0^{\sup} = 0$. By Poisson process definition and since C verifies Eq. (1), we have

$$C_t = Z_t^U + \mathcal{Y}_4 \left(\gamma \int_0^t C_s ds \right). \tag{28}$$

In the same way, since $C^{\sup}$ verifies (20), we have

$$C_t^{\sup} = Z_t^V + \mathcal{Y}_4 \left(\gamma \int_0^t C_s^{\sup} ds \right). \tag{29}$$

Let Q be the first time when the $C^{\sup}$ and C processes are distinct:

$$Q := \inf \left(t \geq 0, C_t^{\sup} \neq C_t \right),$$

and, let R_Q, be the first time when the $C^{\sup}$ and C processes meet again:

$$R_Q := \inf \left(t \geq Q, C_t^{\sup} = C_t \right).$$

Note that at $t = Q$, $\mathcal{Y}_4 \left(\gamma \int_0^t C_s ds \right) = \mathcal{Y}_4 \left(\gamma \int_0^t C_s^{\sup} ds \right)$. Since C and $C^{\sup}$ have jumps of size one, between Q and R_Q, one of the two processes stays

necessarily over the other one. Using inequality (21) and equations (28) and (29), we deduce that for all $t \in (Q, R_Q)$,

$$C_t^{\sup} > C_t.$$

Hence, for all $t \in (Q, R_Q)$,

$$\mathcal{Y}_4\left(\gamma \int_0^t C_s^{\sup} ds\right) \geq \mathcal{Y}_4\left(\gamma \int_0^t C_s ds\right).$$

From this and from inequality (21), we deduce that for all $t \in (0, R_Q)$,

$$C_t^{\sup} \geq C_t.$$

By strong Markov property, we conclude that the above inequality is valid for all times $t \in \mathbb{R}_+$.
In the same way as in Eq. 9, we obtain the upper bound for the F process. Using the same notation as above, we can write that

$$F_t = f_0 - \sum_{k \geq 1} \mathbb{1}_{\{U_k^2 \leq t\}} - \mathcal{Y}_1\left(\alpha_1 \int_0^t F_s ds\right).$$

Let Q^F be the first time when the $F^{\sup}$ and F processes are distinct:

$$Q^F := \inf\left(t \geq 0, F_t^{\sup} \neq F_t\right),$$

and, let $R_{Q^F}^F$, be the first time when the $F^{\sup}$ and F processes meet again:

$$R_{Q^F}^F := \inf\left(t \geq Q^F, F_t^{\sup} = F_t\right).$$

Note that at $t = Q^F$, $\mathcal{Y}_1\left(\alpha_1 \int_0^t F_s ds\right) = \mathcal{Y}_1\left(\alpha_1 \int_0^t F_s^{\sup} ds\right)$. Since F and $F^{\sup}$ have jumps of size one, between Q^F and $R_{Q^F}^F$, one of the two processes stays necessarily over the other one. Hence, we deduce that for all $t \in (0, R_{Q^F}^F)$,

$$F_t^{\sup} \geq F_t.$$

By strong Markov property, we conclude that the above inequality is valid for all times $t \in \mathbb{R}_+$.

□

We now assess the first moment of the extinction time of the upper bound process. In the same way, we define τ^{sup} as

$$\tau^{sup} := \inf\left\{t, F_t^{sup} = 0 | F_0^{\sup} = f_0\right\}.$$

Proposition 5 (First moment of $C_{\tau^{sup}}^{\sup}$) *Under Hypotheses 1 and 3, we have:*

– *if* $\gamma > 0$*:*

$$\mathbb{E}\left[C^{sup}_{\tau^{sup}}\right] = \frac{(\alpha_1+\beta_1+\alpha_2)f_0}{\gamma}\left[\alpha_1 f_0 \sum_{k=0}^{f_0-1}\binom{f_0-1}{k}(-1)^{k+1}\frac{1}{\gamma-\alpha_1(k+1)} - 1\right] \tag{30}$$

– *if* $\gamma = 0$*:*

$$\mathbb{E}\left[C^{sup}_{\tau^{sup}}\right] = \frac{\alpha_1+\beta_1+\alpha_2}{\alpha_1} f_0 \sum_{i=1}^{f_0}\frac{1}{i}. \tag{31}$$

Proof Since τ^{sup} and C^{sup} are independent, we deduce by conditioning with respect to τ^{sup} that

$$\mathbb{E}\left[C^{sup}_{\tau^{sup}}\right] = \int_0^{+\infty} \mathbb{E}\left[C^{sup}_t\right] f_{\tau^{sup}}(t)dt, \tag{32}$$

where $f_{\tau^{sup}}$ is the density probability of τ^{sup}.
First, we suppose that $\gamma > 0$. Hence, C^{sup} is a birth process with immigration and we use the classical result that C^{sup}_t follows a negative binomial law $\mathcal{BN}\left(\frac{\alpha_1+\beta_1+\alpha_2}{\gamma} f_0, e^{-\gamma t}\right)$. In particular, for all $t \geq 0$,

$$\mathbb{E}\left[C^{sup}_t\right] = \frac{\alpha_1+\beta_1+\alpha_2}{\gamma} f_0(e^{\gamma t}-1). \tag{33}$$

Since F^{sup} is linear, we apply Proposition 2 and obtain

$$f_{\tau^{sup}}(t) = \alpha_1 f_0 e^{-\alpha_1 t}(1-e^{-\alpha_1 t})^{f_0-1}\mathbb{1}_{[0,+\infty)}(t). \tag{34}$$

Then, using (33) and (34), we deduce from (32) that

$$\mathbb{E}\left[C^{sup}_{\tau^{sup}}\right] = \alpha_1\frac{\alpha_1+\beta_1+\alpha_2}{\gamma} f_0^2 \int_0^{\infty}(e^{\gamma t}-1)e^{-\alpha_1 t}(1-e^{-\alpha_1 t})^{f_0-1}dt < \infty$$

under Hypothesis 3. We have

$$\alpha_1 f_0 \int_0^{\infty} e^{-\alpha_1 t}(1-e^{-\alpha_1 t})^{f_0-1}dt = \left[(1-e^{-\alpha_1 t})^{f_0}\right]_0^{\infty} = 1, \tag{35}$$

and

$$\begin{aligned}\int_0^{\infty} e^{(\gamma-\alpha_1)t}(1-e^{-\alpha_1 t})^{f_0-1}dt &= \sum_{k=0}^{f_0-1}\binom{f_0-1}{k}(-1)^k\int_0^{\infty} e^{(\gamma-\alpha_1(k+1))t}dt \\ &= \sum_{k=0}^{f_0-1}\binom{f_0-1}{k}(-1)^{k+1}\frac{1}{\gamma-\alpha_1(k+1)}.\end{aligned} \tag{36}$$

From Eq. (35) and (36), we deduce relation (30).
If $\gamma = 0$, then C^{sup} is a pure immigration process and follows a Poisson law $\mathcal{P}\left((\alpha_1+\beta_1+\alpha_2)f_0 t\right)$ at time $t \geq 0$. Using the same approach, we obtain that

$$\mathbb{E}\left[C^{\sup}_{\tau^{\sup}}\right] = \int_0^{+\infty}(\alpha_1+\beta_1+\alpha_2)f_0 t f_{\tau^{\sup}}(t)dt = (\alpha_1+\beta_1+\alpha_2)f_0\mathbb{E}\left[\tau^{\sup}\right].$$

We obtain Eq. (31) using Proposition 2.

□

We immediately deduce the following corollary

Corollary 1 *Under Hypothesis 1, we have* $\mathbb{E}\left[\tau^{f_0}\right] < \infty$. *In addition, under Hypothesis 3, we have* $\mathbb{E}\left[C_{\tau^{f_0}}\right] < \infty$.

Proof Since, according to Proposition 4, for all $t \geq 0$, $F_t^{\sup} \geq F_t$, we first deduce that, necessarily, $\tau^{\sup} \geq \tau^{f_0}$. Then, since, according to Proposition 2, $\mathbb{E}\left[\tau^{\sup}\right] < \infty$, we can conclude that $\mathbb{E}\left[\tau^{f_0}\right] < \infty$.
In the same way, since $C^{\sup}$ and C are both increasing processes, we obtain from Proposition 4, that

$$C^{\sup}_{\tau^{\sup}} \geq C_{\tau^{\sup}} \geq C_{\tau^{f_0}}.$$

Using Proposition 5, we conclude that $\mathbb{E}\left[C_{\tau^{f_0}}\right] < \infty$.

□

3.2.3 Numerical scheme for the mean extinction time and mean number of proliferative cells at the extinction time

Let the domain $\mathcal{D}$ be defined as

$$\mathcal{D} := [\![1, f_0]\!] \times \mathbb{N}. \tag{37}$$

We can compute the moment of τ^{f_0} and $C_\tau^{f_0}$ using the martingale problem (3). We introduce the following problem: find the value $g(f_0, 0)$ where g is solution of

$$\forall (f, c) \in \mathcal{D},\ \mathcal{L}g(f, c) = \alpha \text{ and } g(0, c) = g_0(c),\ \forall c \in \mathbb{N} \tag{38}$$

where the g_0 function and α scalar are to be chosen according to whether we want to obtain $\mathbb{E}\left[\tau^{f_0}\right]$ or $\mathbb{E}\left[C_{\tau^{f_0}}\right]$.

1. For $\mathbb{E}\left[\tau^{f_0}\right]$, we take, for all $c \in \mathbb{N}$, $g_0(c) = 0$ and $\alpha = -1$.
2. For $\mathbb{E}\left[C_{\tau^{f_0}}\right]$, we take, for all $c \in \mathbb{N}$, $g_0(c) = c$ and $\alpha = 0$.

We detail formally why $\mathbb{E}\left[\tau^{f_0}\right] = g(f_0, 0)$. Instantiating the martingale problem (3) at time $t = \tau^{f_0}$ and taking the expectation, we obtain:

$$\mathbb{E}\left[g(X_{\tau^{f_0}})\right] = \mathbb{E}\left[g(X_0)\right] - \mathbb{E}\left[\int_0^{\tau^{f_0}} \mathcal{L}g(X_s)ds\right].$$

Note that, for all $s \in (0, \tau^{f_0})$, $X_s \in \mathcal{D}$. Since $\alpha = -1$, $\mathcal{L}g = -1$ for all $(f, c) \in \mathcal{S}$, and, since $g(X_{\tau^{F_0}} = (0, C_{\tau^{f_0}})) = 0$, we deduce that $\mathbb{E}\left[\tau^{f_0}\right] = \mathbb{E}\left[g(X_0)\right] = g(f_0, 0)$.
Actually, the martingale problem (3) is only valid for compactly supported functions, which is not necessarily the case for g. Nevertheless, we are going to show directly that the solution of system (38) on a truncated domain converges to $\mathbb{E}\left[\tau^{f_0}\right]$. The truncated problem is also motivated by numerical issues.
We can notice that system (38), which is similar to the Kolmogorov backward equation, is unclosed, and there exists no analytical solution. We can obtain a numerical estimate for the scalar $g(f_0, 0)$ using a domain truncation method, as proposed in Munsky and Khammash (2006); Kuntz (2017).

Domain truncation method We introduce the killed chain Z, similar to X on $\mathcal{D}$, whose transition matrix $Q^Z := (q^Z(x,y))_{x,y\in\mathcal{S}}$ coincides with Q on $\mathcal{D}$:

$$q^Z(x,y) = q(x,y), \forall x \in \mathcal{D}, y \in \mathcal{S}, \text{ and } q^Z(x,y) = 0, \forall x \notin \mathcal{D}, y \in \mathcal{S}.$$

Lemma 2.4 of Kuntz (2017) ensures us that the chains X and Z are identical up to the first exit time from domain $\mathcal{D}$, i.e. at time $t = \tau^{f_0}$.
In a second step, we introduce the truncated state space $\mathcal{S}^r$ (following Kuntz (2017)), defined as: for all $r \in \mathbb{N}^*$,

$$S^r := [\![0, f_0]\!] \times [\![0, r]\!] \cup \{(0, r+1), (1, r+1)\} \setminus \{(0,0)\} \tag{39}$$

and the truncated domain $\mathcal{D}^r := S^r \cap \mathcal{D}$.
We also construct the Markov chain Z^r, similar to Z on domain $\mathcal{D}^r$ and killed outside $\mathcal{D}^r$. The chains Z and Z^r are identical up to the first exit time from domain $\mathcal{D}^r$,

$$\tau_r^{f_0} := \inf\left(t \text{ such that } Z_t^r \notin \mathcal{D}^r\right) = \tau^{f_0} \wedge \tau_{\mathcal{S}^r},$$
$$\text{where } \tau_{\mathcal{S}^r} := \inf\left(t \text{ such that } Z_t^r \notin \mathcal{S}^r\right). \tag{40}$$

We include the state $(0, r+1), (1, r+1)$ in domain S^r to ensure that $\tau_{\mathcal{S}^r} \neq \tau^{f_0}$. In Figure 7 we draw the different domains $\mathcal{D}, S^r, \mathcal{D}^r$, and we sketch typical trajectories of the X process and the auxiliary processes that we have defined on each domain, namely Z and Z^r. The Z (resp. Z^r) process coincides with X as long as X stays in domain $\mathcal{D}$ (resp. $\mathcal{D}^r$) and is stopped when X leaves domain $\mathcal{D}$ (resp. $\mathcal{D}^r$).

Since $\mathcal{S}^r$ is a strictly increasing sequence of sets such that $\cup_r \mathcal{S}^r = \mathcal{S}$, $\tau_{\mathcal{S}_r}$ goes to infinity a.s. when r goes to infinity. Since, according to Corollary 1, $\tau^{f_0} < +\infty$, $\tau_r^{f_0}$ converges to τ^{f_0} a.s. when r goes to infinity. Using that C is an increasing process, we also deduce the a.s. convergence of the sequence of random variables $C_{\tau_r^{f_0}}$ to $C_{\tau^{f_0}}$ when r goes to infinity. We show in the next proposition that the convergence holds in mean for both $\tau_r^{f_0}$ and $C_{\tau_r^{f_0}}$.

Proposition 6 (Domain truncation relative error) *Let $p \in \mathbb{N}^*$, such that $\mathbb{E}[(C_{\tau^{f_0}})^p] < \infty$, and, let $r \in \mathbb{R}_+^*$ and $\epsilon_r := \frac{\mathbb{E}[(C_{\tau^{f_0}})^p]}{r^p}$. Then, we have*

$$\frac{|\mathbb{E}\left[\tau^{f_0}\right] - \mathbb{E}\left[\tau_r^{f_0}\right]|}{\mathbb{E}\left[\tau^{f_0}\right]} \leq \epsilon_r \text{ and } \frac{|\mathbb{E}\left[C_{\tau_{f_0}}\right] - \mathbb{E}\left[C_{\tau_{f_0}^r}\right]|}{\mathbb{E}\left[C_{\tau_{f_0}}\right]} \leq \epsilon_r.$$

Proof We combine the study of $\tau_r^{f_0}$ and $C_{\tau_r^{f_0}}$ by introducing $h(\tau_r^{f_0})$, where the h function is either $h(x) = x$ or $h(x) = C_x$. According to Corollary 1, we get $\mathbb{E}\left[h(\tau_r^{f_0})\right] < \infty$ for both cases. As $\mathbb{P}\left[\tau_{\mathcal{S}_r} = \tau^{f_0}\right] = 0$, we can write that

$$\mathbb{P}\left[\tau_r^{f_0} = \tau^{f_0}\right] = 1 - \mathbb{P}\left[\tau_r^{f_0} = \tau_{\mathcal{S}_r}\right]. \tag{41}$$

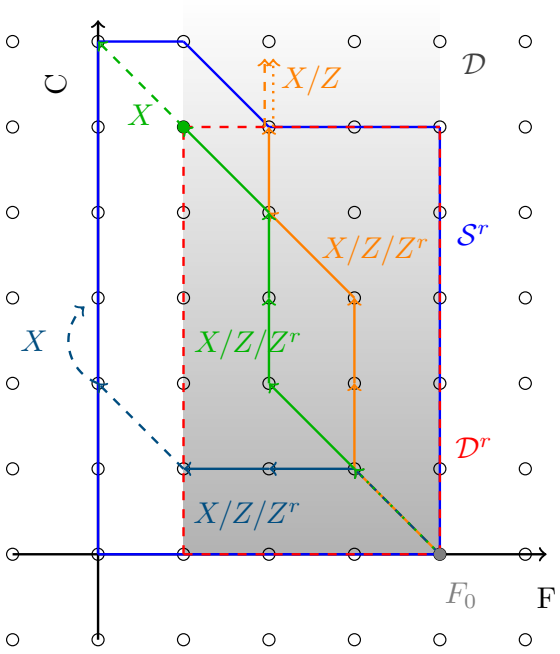

Fig. 7 Domains and processes used in the finite state projection method, related to Proposition 6. In shaded gray, we plot the infinite domain $\mathcal{D}$ defined in Eq. (37). The solid blue line delimits the boundary of domain $\mathcal{S}^r$, defined in Eq. (39). The red dashed line delimits the boundary of domain $\mathcal{D}^r$, corresponding to the intersection of $\mathcal{D}$ and $\mathcal{S}^r$. The blue, green and orange lines illustrate three typical trajectories of the processes X, Z, Z^r.

Conditioning $\mathbb{E}\left[h(\tau_r^{f_0})\right]$ with respect to $\tau_r^{f_0}$ and using its definition (see (40)), we deduce:

$$\begin{aligned}
&\mathbb{E}\left[h(\tau_r^{f_0})\right] \\
&= \mathbb{E}\left[h(\tau_r^{f_0})|\tau_r^{f_0} = \tau^{f_0}\right]\mathbb{P}\left[\tau_r^{f_0} = \tau^{f_0}\right] + \mathbb{E}\left[h(\tau_r^{f_0})|\tau_r^{f_0} = \tau_{\mathcal{S}_r}\right]\mathbb{P}\left[\tau_r^{f_0} = \tau_{\mathcal{S}_r}\right] \\
&= \mathbb{E}\left[h(\tau^{f_0})\right]\mathbb{P}\left[\tau_r^{f_0} = \tau^{f_0}\right] + \mathbb{E}\left[h(\tau_{\mathcal{S}_r})\right]\mathbb{P}\left[\tau_r^{f_0} = \tau_{\mathcal{S}_r}\right].
\end{aligned}$$

We have $\tau^{f_0} \geq \tau_r^{f_0}$ for all $r \geq 0$. Hence, $h(\tau^{f_0}) \geq h(\tau_r^{f_0})$ and we obtain:

$$\left|\mathbb{E}\left[h(\tau^{f_0})\right] - \mathbb{E}\left[h(\tau_r^{f_0})\right]\right| = \mathbb{E}\left[h(\tau^{f_0})\right](1 - \mathbb{P}\left[\tau_r^{f_0} = \tau^{f_0}\right]) - \mathbb{E}\left[h(\tau_{\mathcal{S}_r})\right]\mathbb{P}\left[\tau_r^{f_0} = \tau_{\mathcal{S}_r}\right].$$

From equation (41), we deduce first

$$\left|\mathbb{E}\left[h(\tau^{f_0})\right] - \mathbb{E}\left[h(\tau_r^{f_0})\right]\right| = \left(\mathbb{E}\left[h(\tau^{f_0})\right] - \mathbb{E}\left[h(\tau_{\mathcal{S}_r})\right]\right)\mathbb{P}\left[\tau_r^{f_0} = \tau_{\mathcal{S}_r}\right],$$

then

$$\frac{\left|\mathbb{E}\left[h(\tau^{f_0})\right] - \mathbb{E}\left[h(\tau_r^{f_0})\right]\right|}{\mathbb{E}\left[h(\tau^{f_0})\right]} \leq \mathbb{P}\left[\tau_r^{f_0} = \tau_{\mathcal{S}_r}\right].$$

Note that $\mathbb{P}\left[\tau_r^{f_0} = \tau_{\mathcal{S}_r}\right] = \mathbb{P}\left[C_{\tau_r^{f_0}} = r\right] = \mathbb{P}\left[C_{\tau_r^{f_0}} \geq r\right]$. Since C is increasing, $C_{\tau_r^{f_0}} \leq C_{\tau^{f_0}}$, hence we obtain

$$\mathbb{P}\left[\tau_r^{f_0} = \tau_{\mathcal{S}_r}\right] \leq \mathbb{P}\left[C_{\tau^{f_0}} \geq r\right].$$

Finally, Chebychev inequality give us that,

$$\mathbb{P}\left[\tau_r^{f_0} = \tau_{\mathcal{S}_r}\right] \leq \frac{\mathbb{E}[(C_{\tau^{f_0}})^p]}{r^p},$$

which ends the proof.

□

Pseudo-code According to Proposition 4, we first have that

$$C_{\tau_{F_0}} \leq C^{\sup}_{\tau^{\sup}} \text{ a.s. },$$

then together with Proposition 6 for $p = 1$, we obtain

$$\frac{|\mathbb{E}\left[\tau^{f_0}\right] - \mathbb{E}\left[\tau_r^{f_0}\right]|}{\mathbb{E}\left[\tau^{f_0}\right]} \leq \frac{A}{r} \text{ and } \frac{|\mathbb{E}\left[C_{\tau_{f_0}}\right] - \mathbb{E}\left[C_{\tau_{f_0}^r}\right]|}{\mathbb{E}\left[C_{\tau_{f_0}}\right]} \leq \frac{A}{r},$$

where, if $\gamma > 0$,

$$A = \frac{(\alpha_1 + \alpha_2 + \beta_1) f_0}{\gamma} \left[\alpha_1 f_0 \sum_{k=0}^{f_0-1} \binom{f_0 - 1}{k} (-1)^{k+1} \frac{1}{\gamma - \alpha_1(k+1)} - 1\right] \quad (42)$$

or, if $\gamma = 0$,

$$A = \frac{\alpha_1 + \beta_1 + \alpha_2}{\alpha_1} f_0^2 \sum_{i=0}^{f_0-1} \binom{f_0 - 1}{i} \frac{(-1)^i}{(i+1)^2}. \quad (43)$$

We design the following algorithm to compute a numerical estimate of $g(f_0, 0)$:

Fix f_0, g_0, α, the parameter set $\theta = (\alpha_1, \alpha_2, \beta_1, \gamma)$ and the tolerance error ϵ;
Compute $r = \frac{A}{\epsilon}$ from equation (42) or equation (43) ;
Initialize $g_r(f, r) = 0$ for all $f \in [\![0, f_0]\!]$;
for *c from* $r - 1$ *to* 0 **do**
  $g_r(0, c) \leftarrow g_0(c)$;
  for *f from* 1 *to* f_0 **do**
    $g_r(f, c) \leftarrow \frac{-\alpha + (\alpha_1 f + \beta_1 \frac{fc}{f+c}) g_r(f-1, c+1) + (\gamma c + \alpha_2 f) g_r(f, c+1)}{\gamma c + (\alpha_1 f + \beta_1 \frac{fc}{f+c}) + \alpha_2 f}$;
  end
end
Return $g_r(f_0, 0)$;

Algorithm 1: Numerical estimate of $g(f_0, 0)$

We apply Algorithm 1 to explore the influence of parameters on both the mean extinction time of the precursor cells, $\mathbb{E}\left[\tau^{f_0}\right]$, and the mean number of

proliferative cells at that time, $\mathbb{E}\left[C_{\tau^{f_0}}\right]$ for the nonlinear model.
On the left panel of Figure 8, we can observe that $\mathbb{E}\left[\tau^{f_0}\right]$ decreases like a logistic function with respect to β_1 (in log scale), with a sharp transition for $\beta_1 \approx \alpha_1$. When β_1 tends to zero ($\beta_1 \ll \alpha_1 = 1$), the mean extinction time $\mathbb{E}\left[\tau^{f_0}\right]$ converges to $\mathbb{E}\left[\tau_L^{f_0}\right]$. On the contrary, when β_1 is large ($\beta_1 \gg \alpha_1$), the mean extinction time $\mathbb{E}\left[\tau^{f_0}\right]$ converges to $\mathbb{E}\left[\mathcal{E}\left((\alpha_1+\alpha_2)f_0\right)\right] = \frac{1}{(\alpha_1+\alpha_2)f_0}$, which corresponds to the mean time of the first event (in other words, when β_1 is large, cell event $\mathcal{R}_2$ becomes instantaneous). The various parameter configurations shown in this panel lead to the conclusion that the parameter that affects the most the mean extinction time $\mathbb{E}\left[\tau^{f_0}\right]$ is the auto-amplified transition rate β_1, while the division rates α_2 and γ have relatively less effect. Moreover, it is clear from the analytical solutions of the linear model, that the initial number of precursor cells f_0 and the spontaneous transition rate α_1 have a major impact on $\mathbb{E}\left[\tau^{f_0}\right]$.
A logistic-shaped function is observed as well for $\mathbb{E}\left[C_{\tau^{f_0}}\right]$ (middle panel of Figure 8) when β_1 is tuned (log scale), with a sharp transition around $\beta_1 \approx \alpha_1$. When β_1 is small, cells have time to divide before extinction (leading to a higher level of $\mathbb{E}\left[C_{\tau^{f_0}}\right]$) while when β_1 is large, the main cell event is $\mathcal{R}_2$ and few cells can divide before extinction, the limit value being $f_0 + \frac{\alpha_2}{\alpha_1+\alpha_2}$ when $\beta_1 \to \infty$.
On the right panel of Figure 8, we plot the mean number of proliferative cells at the extinction time as a function of the mean extinction time, when β_1 is tuned. These two quantities appear to be roughly linearly correlated, with a slope that depends on the other parameter values. The inserted zoom around $(0, f_0)$ shows that submodel $(\mathcal{R}_1, \mathcal{R}_2, \mathcal{R}_3)$ can surprisingly lead to a higher mean number of proliferative cells than submodel $(\mathcal{R}_1, \mathcal{R}_2, \mathcal{R}_4)$ (with unchanged α_2 and γ values). This phenomenon arises for a large β_1 value (and small mean extinction time). In such a case, an asymmetric division in submodel $(\mathcal{R}_1, \mathcal{R}_2, \mathcal{R}_3)$ may arise before a spontaneous transition (with probability $\frac{\alpha_2}{\alpha_1+\alpha_2}$), while a symmetric division in submodel $(\mathcal{R}_1, \mathcal{R}_2, \mathcal{R}_4)$ can only arise after a first spontaneous transition, yet is unlikely to occur for large β_1 and fast extinction. However, for small feedback rate β_1, the possibility of symmetric divisions leads to significantly more proliferative cells at the extinction time, as expected.

4 Parameter calibration

In this section, we calibrate the model parameters using a likelihood approach. We first describe the available experimental dataset, as well as in-silico datasets that we use as a benchmark for our methodology. Then we derive a likelihood function based on the embedded Markov chain from the underlying continuous-time Markov process. We explain how this likelihood is specifically adapted to the data, which are time-free measurements of cell numbers. Finally, we both present the estimation results for each submodel derived from model $(\mathcal{M}_{FC})$

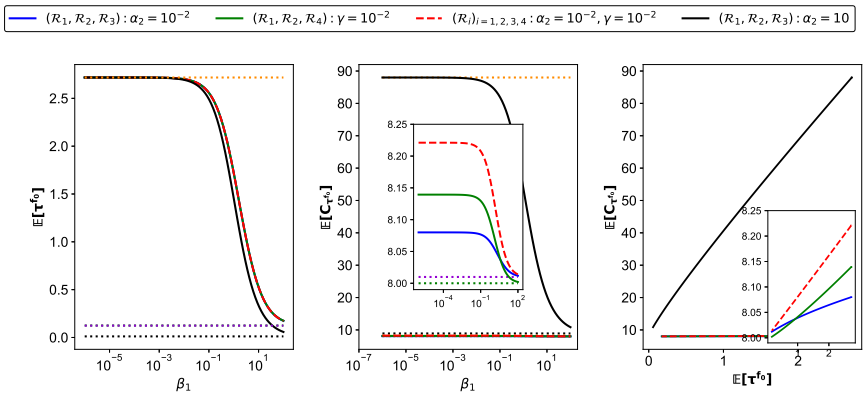

Fig. 8 Mean extinction time and mean number of proliferative cells at the extinction time. Using Algorithm 1 with $\epsilon = 10^{-2}$, we compute the mean extinction time and the mean number of proliferative cells at the extinction time. Left panel: mean extinction time as a function of β_1. Middle panel: mean number of proliferative cells at the extinction time as a function of β_1. Right panel: Mean number of proliferative cells as a function of the mean extinction time, when β_1 varies. In each panel, we use four different parameter configurations as follows. In all cases, $f_0 = 8$ and $\alpha_1 = 1$. Black solid line: submodel $(\mathcal{R}_1, \mathcal{R}_2, \mathcal{R}_3)$ with $\alpha_2 = 10$. Blue solid line: submodel $(\mathcal{R}_1, \mathcal{R}_2, \mathcal{R}_3)$ with $\alpha_2 = 0.01$. Green solid line: submodel $(\mathcal{R}_1, \mathcal{R}_2, \mathcal{R}_4)$ with $\gamma = 0.01$. Red dashed line: model $\mathcal{M}_{FC}$ with $\alpha_2 = \gamma = 0.01$. The orange dotted horizontal lines represent the mean extinction time and number of proliferative cells at the extinction time when $\beta_1 = 0$ (applying formulas in Proposition 3 or, for submodel $(\mathcal{R}_1, \mathcal{R}_3, \mathcal{R}_4)$, simulating the stochastic process). The remaining colored dotted horizontal lines correspond to the mean extinction time and number of proliferative cells at the extinction time when $\beta_1 \to \infty$. The legend insert on the top of the panels specifies the color code. Dotted red: model $(\mathcal{R}_1, \mathcal{R}_2, \mathcal{R}_3, \mathcal{R}_4)$; blue: model $(\mathcal{R}_1, \mathcal{R}_2, \mathcal{R}_3)$ with $\alpha_2 = 0.01$; green: model $(\mathcal{R}_1, \mathcal{R}_2, \mathcal{R}_4)$; black: model $(\mathcal{R}_1, \mathcal{R}_2, \mathcal{R}_3)$ with $\alpha_2 = 10$. For the mean extinction time, the blue and red dotted lines are superimposed.

and carry out a comprehensive comparison between the different models. In addition, we manage to retrieve hidden kinetic information and assess transit times with given confidence intervals, thanks to a practical parameter identifiability analysis as proposed in Raue et al. (2009).

4.1 Dataset description

Experimental dataset Follicles undergoing the activation process have been classified according to three types Braw-Tal and Yossefi (1997); Gougeon and Chainy (1987); Lundy et al. (1999); Meredith et al. (2000). Primordial follicles (Type I or B) have either not yet or just initiated activation; they are composed of a single layer of flattened cells surrounding the oocyte. Primary follicles (Type II or C) have completed initiation; they only contain cuboidal (transitioned) somatic cells organized in less than two layers (this means that some follicles are strictly mono-layered, while in others an extra partially fulled layer is being built-up). In between Types I and II lies a class of transitory follicles (Type IA or B/C), with a mixture of flattened and cuboidal cells

coexisting within a single layer. The progression from Type I to Type II is accompanied with a more or less pronounced increase in the total cell number (flattened plus cuboidal cells) and enlargement in the oocyte (and follicle) diameter (see bottom-right panel of Figure 9).

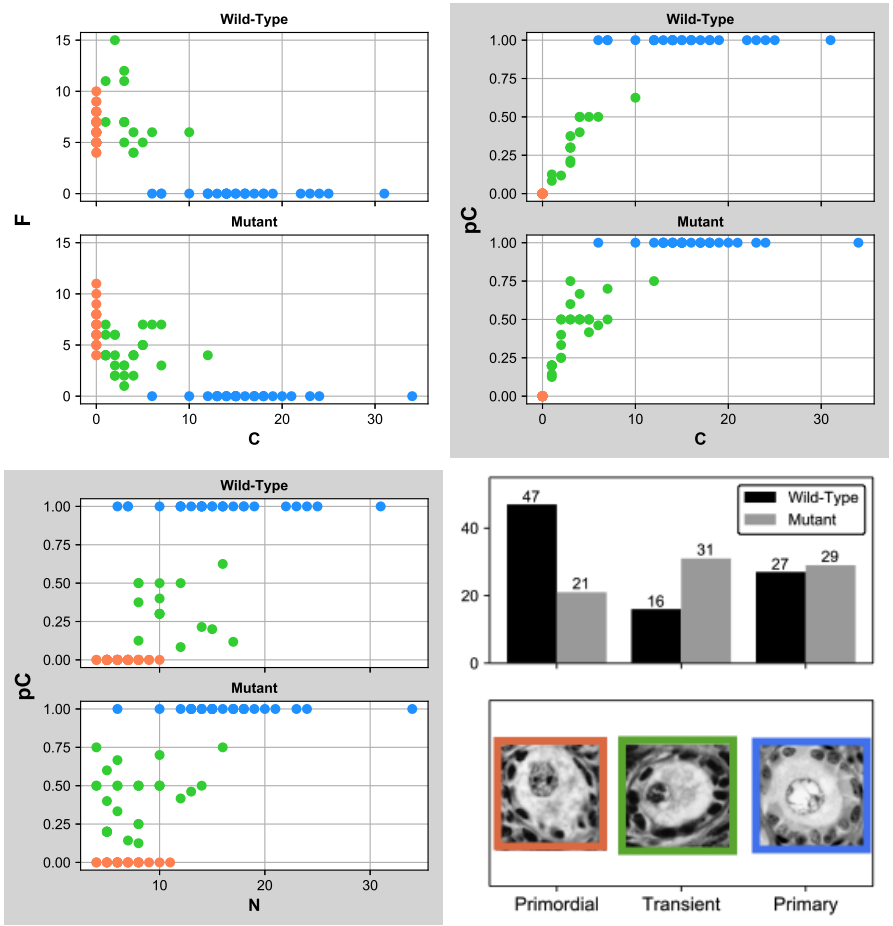

Fig. 9 Description of the experimental dataset. Top-left, top-right and bottom-left panels: experimental data points projected onto three different phase planes, respectively: (F, C), (C, p_c) and (N, p_C), for both the Wild-Type ($\mathbf{x}^{WT}$) and Mutant ($\mathbf{x}^{M}$) subsets. Red points: primary follicles, green points: transitory follicles, blue points: primary follicles. Bottom-right panel: histological slices illustrating the different steps of activation (from left to right: primordial, transitory and primary follicles). Experimental dataset: courtesy of Ken McNatty; histological images: courtesy of Danielle Monniaux.

We have made use of a dataset acquired in sheep fetuses Lundy et al. (1999); Wilson et al. (2001) (courtesy of Ken McNatty), which provides us with precursor and proliferative cell numbers in a sample of follicles distributed into the three activation steps. The dataset is subdivided into two subsets

corresponding to two different sheep strains : the "wild-type" Romney strain and the "mutant" Booroola strain. The latter is characterized by a natural mutation affecting the receptor to growth factor BMP15 and resulting in the alteration of follicle development (see the Introduction section).

We denote respectively by $\mathbf{x}^{WT}$ and $\mathbf{x}^{M}$ the Wild-Type and Mutant subsets such that, for $l \in \mathbf{B} := \{WT, M\}$:

$$\mathbf{x}^l = (x_i)_{i \in [\![1, N^l]\!]},$$

where N^l is either 90 (Wild-Type) or 81 (Mutant), and each element x_i is a vector consisting of the number of precursor and proliferative cells. More specifically, the measures consist of the cell numbers counted on the largest 2D cross-section of histologically fixed follicles of type I, IB or II. This 2D number can be correlated with the total 3D cell number from standard stereological considerations Lundy et al. (1999). In order to deal with a final cell number as close as possible to the number reached at the first time when all flattened cells have transitioned to cuboidal cells (hence to the extinction time in the model), we have only retained the strictly mono-layered type II follicles. Yet, due to the oocyte enlargement and the resulting increased capacity of the first layer, one cannot preclude that a significant amount of cuboidal cells have been generated after the end of the transition period.

Figure 9 illustrates the repartition of the data points according to the follicle type and sheep strain in each phase plane (C, F) (C, p_C), (N, p_C).

In silico datasets In addition to the experimental dataset, we have constructed in silico datasets generated from the simulation of five different submodels: $(\mathcal{R}_1, \mathcal{R}_3)$, $(\mathcal{R}_1, \mathcal{R}_4)$, $(\mathcal{R}_1, \mathcal{R}_2, \mathcal{R}_3)$, $(\mathcal{R}_1, \mathcal{R}_2, \mathcal{R}_4)$ and $(\mathcal{R}_1, \mathcal{R}_3, \mathcal{R}_4)$. We recall that the different submodels are named by the reactions which have corresponding positive reaction rates. All the submodels considered are thus nested models, or reduced model compared to the full model ($\mathcal{M}_{FC}$). For each submodel, we select two parameter sets differing by contrasted values in the division rates α_2 or γ and/or transition rate β_1. We obtain the corresponding 10 datasets by simulating $1,000$ trajectories from the SDE (1), with the Gillespie algorithm Gillespie (1976), starting from the initial condition $(F_0, 0)$ at time $t = 0$ up to the time when $C(t) = 31$ (the value $C(t) = 31$ corresponds to the maximal number of cuboidal cells observed in the experimental dataset). The initial random variable F_0 follows a truncated Poisson law of parameter μ (see Eq.(47)). For each trajectory, we select uniformly randomly one point (f, c) among the state space points reached by the trajectory, so that each in-silico datasets is composed of $N = 1,000$ points. The parameter values are summarized in Table 1.

We note

$$\begin{aligned}\mathbf{S} := \{((\mathcal{R}_1, \mathcal{R}_3), i), i = 1, 2\} \cup \{((\mathcal{R}_1, \mathcal{R}_4), i), i = 1, 2\} \cup \{(\mathcal{R}_1, \mathcal{R}_2, \mathcal{R}_3), i), i = 1, 2\} \\ \cup \{((\mathcal{R}_1, \mathcal{R}_2, \mathcal{R}_4), i), i = 1, 2\} \cup \{((\mathcal{R}_1, \mathcal{R}_3, \mathcal{R}_4), i), i = 1, 2\} \quad (44)\end{aligned}$$

the set of all the in silico datasets.

		α_1	β_1	α_2	γ	μ
$(\mathcal{R}_1, \mathcal{R}_3)$	Dataset $\mathbf{x}^{(\mathcal{R}_1,\mathcal{R}_3),1}$	1	0	0.7	0	5
	Dataset $\mathbf{x}^{(\mathcal{R}_1,\mathcal{R}_3),2}$	1	0	0.007	0	5
$(\mathcal{R}_1, \mathcal{R}_4)$	Dataset $\mathbf{x}^{(\mathcal{R}_1,\mathcal{R}_4),1}$	1	0	0	0.7	5
	Dataset $\mathbf{x}^{(\mathcal{R}_1,\mathcal{R}_4),2}$	1	0	0	0.007	5
$(\mathcal{R}_1, \mathcal{R}_2, \mathcal{R}_3)$	Dataset $\mathbf{x}^{(\mathcal{R}_1,\mathcal{R}_2,\mathcal{R}_3),1}$	1	0.01	0.07	0	5
	Dataset $\mathbf{x}^{(\mathcal{R}_1,\mathcal{R}_2,\mathcal{R}_3),2}$	1	100	0.07	0	5
$(\mathcal{R}_1, \mathcal{R}_3, \mathcal{R}_4)$	Dataset $\mathbf{x}^{(\mathcal{R}_1,\mathcal{R}_3,\mathcal{R}_4),1}$	1	0	0.007	0.7	5
	Dataset $\mathbf{x}^{(\mathcal{R}_1,\mathcal{R}_3,\mathcal{R}_4),2}$	1	0	0.007	0.07	5
$(\mathcal{R}_1, \mathcal{R}_2, \mathcal{R}_4)$	Dataset $\mathbf{x}^{(\mathcal{R}_1,\mathcal{R}_2,\mathcal{R}_4),1}$	1	0.01	0	0.07	5
	Dataset $\mathbf{x}^{(\mathcal{R}_1,\mathcal{R}_2,\mathcal{R}_4),2}$	1	100	0	0.07	5

Table 1 Parameter sets used to generate the in silico datasets

In the sequel (see in particular Figure 11 and 12) these datasets will be used as benchmark tools for the parameter identifiability study and the statistical comparison between the submodels (and complete model). In any case, the set of estimated parameters will match the set of cell events included in the model used to generate the in silico dataset. For instance, we will estimate the values of parameters α_2 and γ on the two datasets generated from submodel $(\mathcal{R}_1, \mathcal{R}_3, \mathcal{R}_4)$.

4.2 Likelihood method

Since the experimental dataset is made of time-free observations, we are going to confront the model to the data using only the information on some state space values taken by the process, without their corresponding time information. This notion is intrinsically related to the embedded Markov chain which we detail below. We will use this Markov chain to compute a likelihood function. Note that the proliferative cell population increases by one cell at each event ($\mathcal{R}_1$, $\mathcal{R}_2$, $\mathcal{R}_3$ or $\mathcal{R}_4$), while the precursor cell population can either remain constant ($\mathcal{R}_3$ or $\mathcal{R}_4$) or decrease by one ($\mathcal{R}_1$ or $\mathcal{R}_2$). The proliferative cell population C can thus be used as an event counter. Indeed, as a continuous-time Markov process, X (defined in Eq. 1) can be decomposed into an embedded Markov chain $(F_n, C_n)_{n\in\mathbb{N}}$ and a sequence of random time jumps $(\tau_n)_{n\in\mathbb{N}}$ with

$$\tau_{n+1} = \tau_n + \mathcal{E}\left((\alpha_1+\alpha_2)F_n + \beta_1\frac{F_nC_n}{F_n+C_n} + \gamma C_n\right), \quad \tau_0 = 0.$$

Note that the sequence of time jumps $(\tau_n)_{n\in\mathbb{N}}$ corresponds exactly to the sequence of time jumps associated with process C, and

$$C(t) = \sum_{n\in\mathbb{N}} \mathbb{1}_{\tau_n\le t}\,, \quad C_n = n\,.$$

Thus, given that $C_n = n$ is deterministic, it is clear that the precursor cell population F_n (alone) is also a (non-homogeneous) Markov chain. To clarify the link with the data, we will index the embedded chain F_n by the number of proliferative cells c, rather than by the number of events that occurred: let F_c be the random variable corresponding to the number of precursor cells given that there are $c \in \mathbb{N}$ proliferative cells. According to the dichotomy between the two division events ($\mathcal{R}_3$, $\mathcal{R}_4$) and the two transition events ($\mathcal{R}_1$, $\mathcal{R}_2$), we deduce the law of F_c at the "pseudo-time" $C = c$ from the law of F_{c-1} at the "pseudo-time" $C = c - 1$ as follows: for all $(f, c) \in \mathcal{S}$,

$$\mathbb{P}\left[F_c = f\right] = \underbrace{q_{f+1,f}(c-1)\mathbb{P}\left[F_{c-1} = f+1\right]}_{\text{transition}} + \underbrace{q_{f,f}(c-1)\mathbb{P}\left[F_{c-1} = f\right]}_{\text{asymmetric/symmetric division}}, \quad (45)$$

where

$$q_{f+1,f}(c) = \frac{\alpha_1(f+1) + \beta_1 \frac{(f+1)c}{f+1+c}}{(\alpha_2+\alpha_1)(f+1) + \gamma c + \beta_1 \frac{(f+1)c}{f+1+c}},$$

$$q_{f,f}(c) = \frac{\alpha_2 f + \gamma c}{(\alpha_2+\alpha_1)f + \gamma c + \beta_1 \frac{fc}{f+c}}. \quad (46)$$

Hence $(F_c)_{c\in\mathbb{N}}$ is a non-homogeneous discrete time Markov chain. Notice that the law of $C_{\tau^{F_0}}$, the number of proliferative cells at the extinction time of the precursor cells, corresponds to the law of the first "pseudo-time" c such that $F_c = 0$, e.g. $C_{\tau^{F_0}} = \inf\{c \in \mathbb{N}^*,\, F_c = 0\}$. Hence, one can use the same estimates (Eq. (42) or Eq. (43)) used in the previous section to analyze the law of $C_{\tau^{F_0}}$, or to reconstruct a numerical approximation of the mean of $C_{\tau^{F_0}}$.

In addition to Eq. (45), to compute the law of (F_c), we need to specify an initial condition F_0. We suppose that the initial number of precursor cells follows a truncated Poisson law of parameter $\mu \in \mathbb{R}_+$ defined as, for all $f \in \mathbb{N}^*$,

$$\mathbb{P}\left[F_0 = f\right] = \frac{\mu^f}{(e^\mu - 1)f!}. \quad (47)$$

Then, we can use Eq. (45) to compute $\mathbb{P}[F_c = f]$ by recurrence from the initial probability vector $(\mathbb{P}[F_0 = i])_{i\in[\![0,c+f]\!]}$. Hence, we have built a discrete time Markov chain $(F_c)_{c\in\mathbb{N}}$ from model $(\mathcal{M}_{FC})$ adapted to our time-free observations.

As can be seen from Eq. (46), the timescale cannot be inferred, so that we fix arbitrarily $\alpha_1 = 1$, whatever the dataset, to obtain dimensionless parameters. The time unit of the remaining parameters is thus relative to the timescale of one spontaneous transition event. As far as the experimental and in silico datasets, except α_1, the estimated parameter values may depend on the specific dataset (experimental or in silico), which we highlight by the following notations for the parameter sets: $\theta^l = (\beta_1^l, \alpha_2^l, \gamma^l, \mu^l) \in \Theta \subset (\mathbb{R}_+)^3 \times [1, +\infty)$, $l \in \mathbf{B} \cup \mathbf{S}$.

Finally, we suppose that all data points are independent of one another, and that the observations are free of measurement errors, and we ignore inter-individual variability.

We obtain the following likelihood function for both the experimental and in silico datasets: for $l \in \mathbf{B} \cup \mathbf{S}$,

$$\mathcal{L}(\mathbf{x}^l; \theta) := \mathbb{P}\left[\mathbf{x}^l | \theta\right] = \prod_{i=1}^{N^l} \mathbb{P}\left[F_{c_i} = f_i | \theta\right].$$

For each submodel $m \in \{(\mathcal{R}_1, \mathcal{R}_4), (\mathcal{R}_1, \mathcal{R}_3), ...\}$ described in the previous section, the optimal parameter values are given by the maximum likelihood estimator $\hat{\theta}^l_m$ (MLE), which we compute by minimizing the negative log-likelihood, for $l \in \mathbf{B} \cup \mathbf{S}$:

$$\hat{\theta}^l_m := \arg\min_{\theta \in \Theta^m} \left(-\log\left(\mathcal{L}(\mathbf{x}^l; \theta)\right)\right),$$

where Θ^m is a subset of Θ constructed by fixing all the parameter sets related to the nonpresent events to the singletons $\{0\}$: for instance, in submodel $(\mathcal{R}_1, \mathcal{R}_4)$, we have $\Theta^{(\mathcal{R}_1, \mathcal{R}_4)} = \{0\} \times \{0\} \times \mathbb{R}_+ \times [1, +\infty)$.
To compute the minimum, we use a derivative-free optimization algorithm: the Differential Evolution (DE) algorithm Storn and Price (1997). In the following, we describe the whole procedure for the complete model $m = (\mathcal{R}_1, \mathcal{R}_2, \mathcal{R}_3, \mathcal{R}_4)$ with the experimental dataset ($l \in \mathbf{B}$). The algorithm starts from an initial population in which each individual is represented by a set of real numbers $(\beta_1, \alpha_2, \gamma, \mu)$. Then, the population evolves along successive generations by mutation and recombination processes. At each generation, the likelihood function is used to assess the fitness of the individuals, and only the best individuals are kept in the population. We have set the intrinsic optimization parameters as follows: the initial population has a size of 20 individuals, and the probability of mutation and crossing-over equals to 0.8 and 0.7 respectively. The starting individual parameter sets are defined on a log scale, and drawn from a uniform distribution on $\Theta = [-6, 6]^3 \times [0, 1.5]$. The algorithm was run over 1,000 iterations. To analyze the parameter identifiability, we follow the practical approach based on the profile likelihood estimate (PLE), see for instance Raue et al. (2009). Specifically, we compute the PLE around the MLE $\hat{\theta}^l_m = \left(\widehat{\beta_1}^l_m, \widehat{\alpha_2}^l_m, \widehat{\gamma}^l_m, \widehat{\mu}^l_m\right)$ for each ith component $\hat{\theta}^l_{m,i}$, $i \in [\![1, 4]\!]$, as follows. We design a grid G_i around the best parameter value $\hat{\theta}^l_{m,i}$ with a fixed step size (see Table 5 in Appendix 6.1 for details), and re-optimize the remaining parameters using the DE algorithm with the same optimization parameters (mut=0.8, crossp=0.7, popsize=20, its = 1,000) and initial parameter sets defined on a log scale, and drawn from a uniform distribution on $[-6, 6]^3$ for parameters β_1, α_2 and γ, and on $[-1 + \log(\hat{\mu}^l_m), \log(\hat{\mu}^l_m) + 1]$ for parameter μ. For each parameter $\hat{\theta}^l_{m,i}$, we obtain a MLE vector $\hat{\theta}^l_m | [\theta^l_{m,i} = x]$, with $x \in G_i$:

$$\hat{\theta}^l_m | [\theta^l_{m,i} = x] := \arg\min_{\theta \in \Theta^m, \theta^l_{m,i} = x} \left(-\log\left(\mathcal{L}(\mathbf{x}^l; \theta)\right)\right),$$

and its associated PLE (vector) $\mathcal{L}(\mathbf{x}^l; \hat{\theta}^l_m | \theta^l_{m,i})$.
Finally, the pointwise likelihood-based confidence intervals are constructed thanks to the likelihood ratio test, following Raue et al. (2009) ; for each estimated parameter $\hat{\theta}^l_{m,i}$, we select all the parameters $\theta^l_{m,i} = x$ such that:

$$\mathcal{L}(x; \theta | [\theta^l_{m,i} = x]) - \mathcal{L}(x; \hat{\theta}^l_m) < 0.5 * \Delta_\alpha,$$

where $\Delta_{0.95} = \chi^2(0.95, 1) = 3.84$ is the 0.95-quantile of the χ^2 law with 1 degree of freedom.

4.3 Fitting results

In this subsection, we calibrate the model parameters for several submodels derived from model ($\mathcal{M}_{FC}$):

- two-event submodels, including the spontaneous transition event together with either the asymmetric $(\mathcal{R}_1, \mathcal{R}_3)$ or symmetric division $(\mathcal{R}_1, \mathcal{R}_4)$;
- three-event submodels, including both the spontaneous and auto-amplified transition events, together with either the asymmetric $(\mathcal{R}_1, \mathcal{R}_2, \mathcal{R}_3)$ or symmetric $(\mathcal{R}_1, \mathcal{R}_2, \mathcal{R}_4)$ division event;
- the full model $(\mathcal{R}_1, \mathcal{R}_2, \mathcal{R}_4, \mathcal{R}_4)$

In all cases the parameter ruling the initial condition, μ, is estimated.

We follow the procedure described in subsection 4.2 to fit the parameters on the experimental subsets $\mathbf{x}^{WT}$ and $\mathbf{x}^M$ and in-silico datasets introduced in subsection 4.1.

4.3.1 Two-event submodels

The fitting results for submodels $(\mathcal{R}_1, \mathcal{R}_3)$ and $(\mathcal{R}_1, \mathcal{R}_4)$ are shown in Figure 10. For both the Wild-Type and Mutant subsets, a visual inspection shows that submodel $(\mathcal{R}_1, \mathcal{R}_4)$ leads to a "direct" transition, followed by prolonged cell proliferation after precursor cell extinction, while with submodel $(\mathcal{R}_1, \mathcal{R}_3)$, there is a higher probability that the total number of cells increases before precursor cell extinction. This observation is consistent with the fitting results of the in-silico datasets.

In Figure 11, we show the PLE for each estimated parameter. Both the initial condition parameter μ (orange solid lines) and asymmetric division rate α_2 (green solid line) are practically identifiable (in the sense given in Raue et al. (2009)), while parameter γ (blue solid line) is only partially practically identifiable in most cases. From the in silico dataset analyses, we observe that both parameters α_2 $(\mathcal{R}_3)$ and γ $(\mathcal{R}_4)$ are practically identifiable and close to their expected values (less than one $log10$ of difference) when the parameters are of the same order of magnitude than α_1 (Datasets $\mathbf{x}^{(\mathcal{R}_1,\mathcal{R}_3),1}$ and $\mathbf{x}^{(\mathcal{R}_1,\mathcal{R}_4),1}$). In contrast, a small parameter value compared to α_1 leads to a biased parameter estimate, with a huge shift between the estimated and true parameter values (roughly a two $log10$ difference).

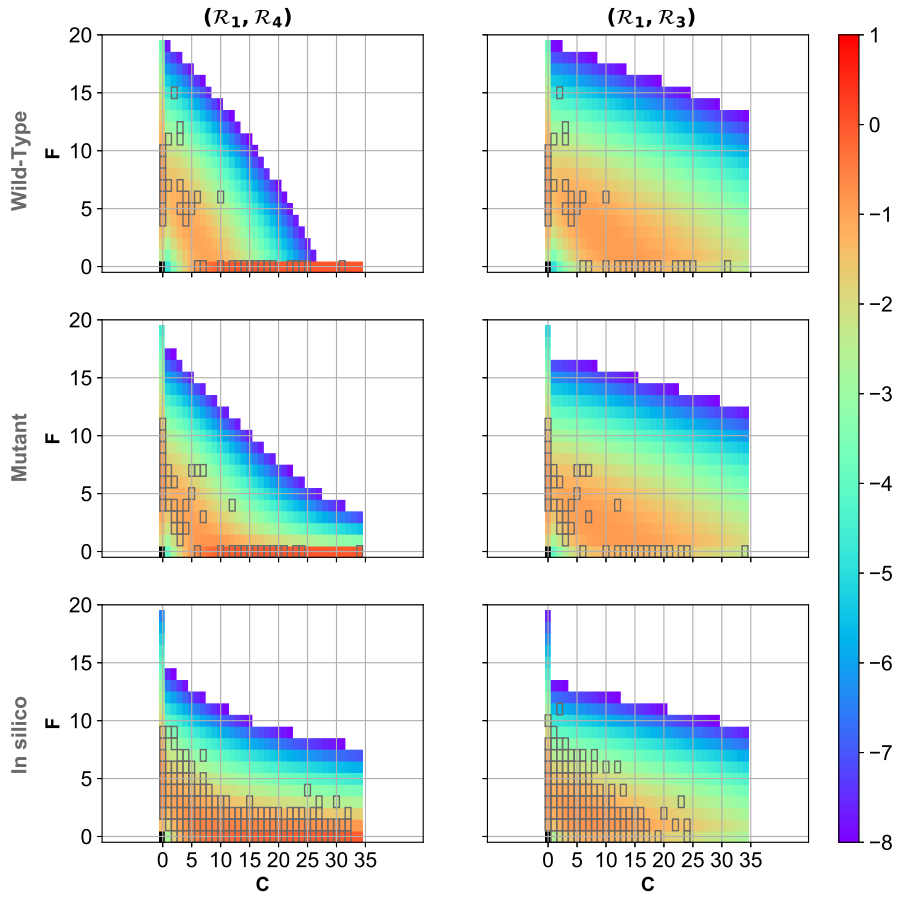

Fig. 10 Two-event submodels: Best fit trajectories. Using Formula 45, we compute each probability $\mathbb{P}[F_c = f]$ for submodel $(\mathcal{R}_1, \mathcal{R}_4)$ with the MLE parameter set $\hat{\theta}^l_m$, $l \in \{WT, M, ((\mathcal{R}_1, \mathcal{R}_4), 1)\}$ (left panels), and submodel $(\mathcal{R}_1, \mathcal{R}_3)$ with the MLE parameter set $\hat{\theta}^l_m$, $l \in \{WT, M, ((\mathcal{R}_1, \mathcal{R}_3), 1)\}$ (right panels). Each dark gray square corresponds to a data point in the datasets $\mathbf{x}^l$, $l \in \{WT, M, ((\mathcal{R}_1, \mathcal{R}_4), 1), ((\mathcal{R}_1, \mathcal{R}_3), 1)\}$.

4.3.2 Three-event submodels and complete model

We turn now to the analysis of three-event submodels $(\mathcal{R}_1, \mathcal{R}_2, \mathcal{R}_3)$, $(\mathcal{R}_1, \mathcal{R}_2, \mathcal{R}_4)$ and $(\mathcal{R}_1, \mathcal{R}_3, \mathcal{R}_4)$) and the complete model $((\mathcal{R}_1, \mathcal{R}_2, \mathcal{R}_3, \mathcal{R}_4)$. Qualitatively, the fitting results for submodel $(\mathcal{R}_1, \mathcal{R}_2, \mathcal{R}_3)$ are similar to those for submodel $(\mathcal{R}_1, \mathcal{R}_3)$ (data not-shown); they are characterized by a high probability to produce ten or more proliferative cells before the precursor cell extinction. The fitting results for submodels $(\mathcal{R}_1, \mathcal{R}_2, \mathcal{R}_4)$ and $(\mathcal{R}_1, \mathcal{R}_3, \mathcal{R}_4)$, as well as for the complete model are rather similar to submodel $(\mathcal{R}_1, \mathcal{R}_4)$; they are characterized by direct cell transition with very little concomitant cell proliferation, followed by prolonged cell proliferation after precursor cell extinction. The fit-

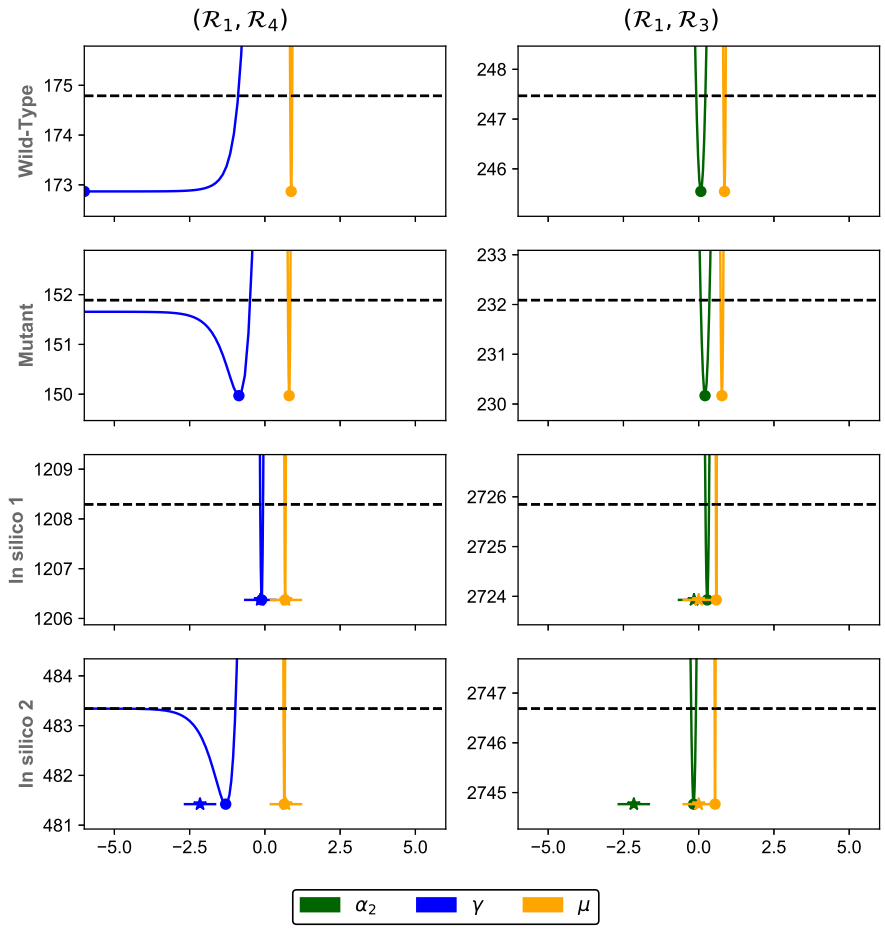

Fig. 11 Two-event submodels: PLE. Each panel represents the PLE, in log10 scale, obtained from the experimental (top panels) and in silico datasets (bottom panels), and either submodel $(\mathcal{R}_1, \mathcal{R}_4)$ (left panels) or $(\mathcal{R}_1, \mathcal{R}_3)$ (right panels). The dashed black line represents the 95%-statistical threshold, while each point represents the optimum value of the likelihood. Orange solid lines: PLE values $\mathcal{L}(\mathbf{x}^l; \hat{\theta}^l_m|\mu)$; blue solid lines: PLE values $\mathcal{L}(\mathbf{x}^l; \hat{\theta}^l_{(\mathcal{R}_1,\mathcal{R}_4)}|\gamma)$; green solid line: PLE values $\mathcal{L}(\mathbf{x}^l; \hat{\theta}^l_{(\mathcal{R}_1,\mathcal{R}_3)}|\alpha_2)$. The colored points are the associated MLE $\hat{\theta}^l_m$. In the bottom panels, the star symbols are the expected (true) parameter values (see Table 1).

ting results for the complete model are shown in the top panel of Figure 13 for both the Wild-type and Mutant subsets. We notice that in the Mutant case, there is a tendency to produce more proliferative cells.

The PLEs for each dataset and each parameter are presented in Figure 12 for the three-event submodels and Figure 13 for the complete model. The corresponding parameter values and confidence intervals for the Wild-Type and Mutant subsets are given in Tables 3 and 4 in the Appendix. As observed for

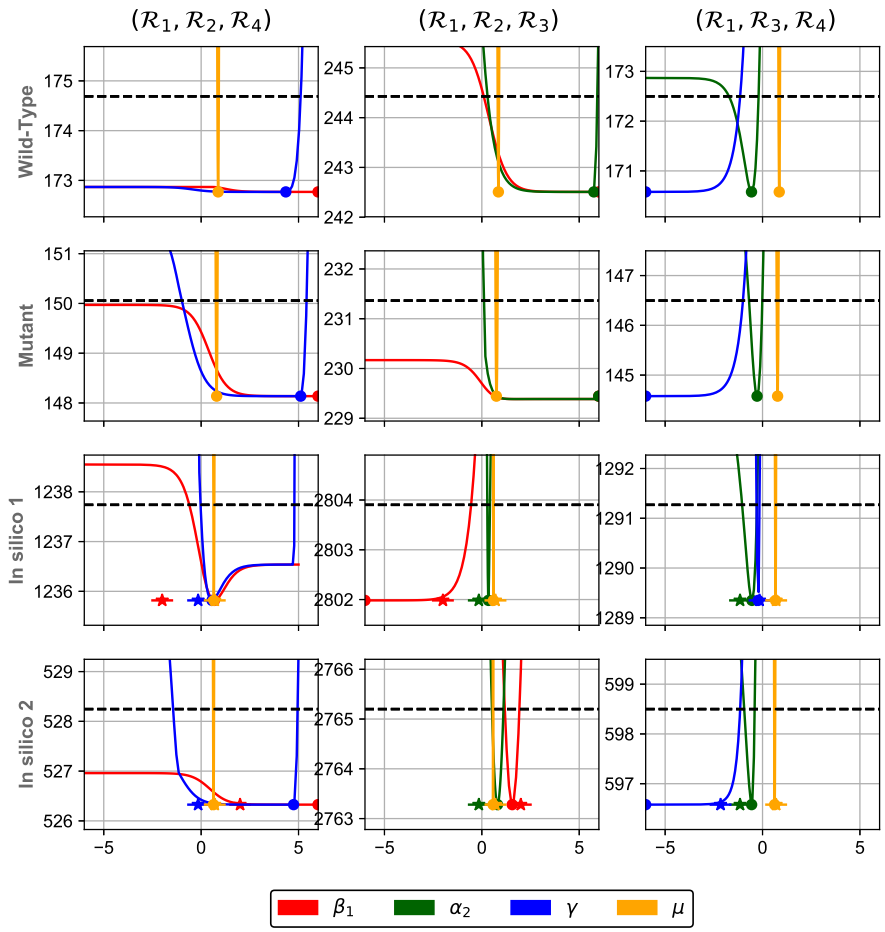

Fig. 12 Three-event submodels: PLE. Each panel represents the PLE, in log10 scale, obtained from the experimental (top panels) and in silico datasets (bottom panels), and either submodel $(\mathcal{R}_1, \mathcal{R}_2, \mathcal{R}_4)$ (left panels), $(\mathcal{R}_1, \mathcal{R}_2, \mathcal{R}_3)$ (center panels), or $(\mathcal{R}_1, \mathcal{R}_3), \mathcal{R}_4)$ (right panels).The dashed black line represents the 95%-statistical threshold, while each point represents the optimum value of the likelihood. Orange solid lines: PLE values $\mathcal{L}(\mathbf{x}^l; \hat{\theta}^l_m|\mu)$; blue solid lines: PLE values $\mathcal{L}(\mathbf{x}^l; \hat{\theta}^l_m|\gamma)$; green solid lines: PLE values $\mathcal{L}(\mathbf{x}^l; \hat{\theta}^l_m|\alpha_2)$; red solid lines: PLE values $\mathcal{L}(\mathbf{x}^l; \hat{\theta}^l_m|\beta_1)$. The colored points are the associated MLE $\hat{\theta}^l_m$. In the bottom panels, the star symbols are the expected (true) parameter values (see Table 1).

the two-event submodels, in each case, the initial condition parameter μ (orange solid lines) is always practically identifiable, and its fitted value is close to the true one for the in silico datasets. In contrast, all other parameters have a lack of identifiability. Specifically, the asymmetric division rate α_2 is practically not identifiable for submodel $(\mathcal{R}_1, \mathcal{R}_2, \mathcal{R}_3)$ with the experimental subsets, while it is identifiable with the in-silico datasets (although the estimated values are slightly biased), which indicates that more data can indeed help to improve

parameter identifiability. Interestingly, when the asymmetric division event is combined with the symmetric division event (submodel $(\mathcal{R}_1, \mathcal{R}_3, \mathcal{R}_4)$) rather than with the auto-amplified transition (submodel $(\mathcal{R}_1, \mathcal{R}_2, \mathcal{R}_3)$), the asymmetric division rate γ becomes identifiable in the experimental subsets, which reveals complex parameter dependencies between the asymmetric division rate α_2 and auto-amplified transition rate β_1. In the complete model, only a very broad confidence interval (3-5 logs) can be obtained for α_2. In most cases, a finite confidence interval for the symmetric division rate γ cannot be inferred from the experimental data, we can just get an upper-bound. The fitting results obtained with the models including event $\mathcal{R}_4$ suggest a possible explanation: since the transition and proliferation events are rather uncoupled, and occur sequentially (first transition, then proliferation), the proliferation rate can just be constrained to be small enough so that proliferation does almost not take place before cell precursor extinction. After precursor cell extinction, the only possible remaining event is the symmetric division event $\mathcal{R}_4$, whose timescale cannot be constrained by the time-free data. This explanation is confirmed by the dependencies of β_1 on γ for submodel $(\mathcal{R}_1, \mathcal{R}_2, \mathcal{R}_4)$, shown in Figure 17 in the Appendix. The optimum value $\widehat{(\beta_1)}^l_m|\gamma$, computed from the PLE of γ (minimizing the likelihood with γ fixed, see the blue lines in the top panels of Figure 12 and bottom panels of Figure 13), increases linearly with γ as soon as the symmetric division rate gets upper than 1 (hence greater than α_1). Finally, the self-amplified transition rate β_1 is not-identifiable in most cases, and even not constrained by any upper-bound for the experimental subsets. We note that in the complete model, the self-amplified transition rate β_1 is constrained to be greater than $\approx 10^{0.66}$ in the Wild-type case, while it is unconstrained in the Mutant case (with a slightly higher probability around $10^{0.44}$).

4.3.3 Comparison of models

We now perform the comparison between the different submodels with either two or three cell events and the complete model ($\mathcal{M}_{FC}$).

The AIC and BIC analyses performed to compare the submodels are summarized in Table 2. The AIC and BIC criteria suggest that the best model associated with the Wild-Type subset is the complete model, while the best model associated with the Mutant subset is the three-event linear submodel $(\mathcal{R}_1, \mathcal{R}_3, \mathcal{R}_4)$.

The reader can refer to Burnham and Anderson (2003) (Chapter 6) for a detailed presentation of the rule of thumb, classically used to analyze the $\Delta_i^{AIC} := AIC_i - AIC_{\min}$ and $\Delta_i^{BIC} = BIC_i - BIC_{\min}$ values, where i is the index of the ith model. For the Wild-Type subset, both ΔAIC and ΔBIC suggest that a suitable alternative ($2 < \Delta < 7$) to the complete model are models $(\mathcal{R}_1, \mathcal{R}_4)$, and $(\mathcal{R}_1, \mathcal{R}_3, \mathcal{R}_4)$, while model $(\mathcal{R}_1, \mathcal{R}_2, \mathcal{R}_4)$ is less relevant ($7 < \Delta < 9$) and the remaining models $(\mathcal{R}_1, \mathcal{R}_3)$, $(\mathcal{R}_1, \mathcal{R}_2, \mathcal{R}_3)$ can be safely ruled out ($\Delta > 10$). For the Mutant subset, the complete model is almost as probable ($\Delta AIC < 2$) as the best model $(\mathcal{R}_1, \mathcal{R}_3, \mathcal{R}_4)$, while models

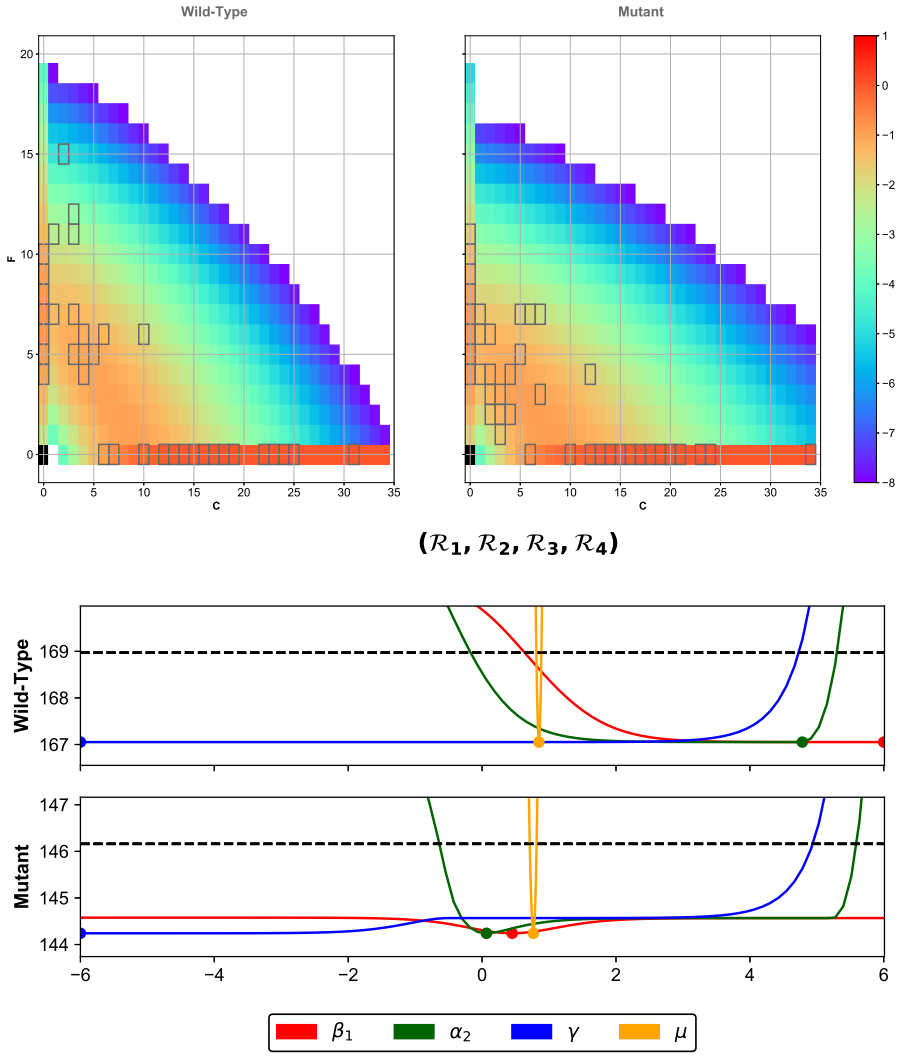

Fig. 13 Complete model: Best fit trajectories and PLE. Top panels: using Formula (45), we compute each probability $\mathbb{P}[F_c = f]$ for the complete model with the MLE $\hat{\theta}^l_m$, $l \in \mathbf{B}$ presented in Tables 3 and 4 (left panel: Wild-Type; right panel: Mutant). Each dark gray square corresponds to one data point in the experimental subsets $\mathbf{x}^l$, $l \in \mathbf{B}$. Middle and bottom panels: each panel represents the PLE, in log10 scale, obtained from the two experimental subsets (middle panel: Wild-Type; bottom panel: Mutant) and for parameters $\beta_1, \alpha_2, \gamma, \mu$ (see the legend of Figure 12). The dashed black line represents the 95%-statistical threshold, while each colored filled circle represents the optimum value of the likelihood.

$(\mathcal{R}_1, \mathcal{R}_4)$ and $(\mathcal{R}_1, \mathcal{R}_2, \mathcal{R}_4)$ are less relevant $(6 < \Delta < 9)$ and models $(\mathcal{R}_1, \mathcal{R}_3)$, $(\mathcal{R}_1, \mathcal{R}_2, \mathcal{R}_3)$ can be safely ruled out as well $(\Delta > 10)$. These results are confirmed by the AIC and BIC weight analyzes. For each dataset and criterion (AIC or BIC), we order the AIC/BIC weights from the highest to the lowest

values and sum them up. We retain as acceptable all the models such that the sum is upper than the p-value 0.95. The AIC-based selection retains the linear $(\mathcal{R}_1, \mathcal{R}_3, \mathcal{R}_4)$ and complete models for both the Wild-Type and Mutant subsets (in both cases, p-value = 0.97), whereas the BIC-based selection retains the two linear models $(\mathcal{R}_1, \mathcal{R}_4)$ and $(\mathcal{R}_1, \mathcal{R}_3, \mathcal{R}_4)$ and the complete model (WT p-value = 0.97, M p-value = 0.96).

Both rejected submodels $(\mathcal{R}_1, \mathcal{R}_3)$, $(\mathcal{R}_1, \mathcal{R}_2, \mathcal{R}_3)$ have indeed a negative log-likelihood far away from the other models, which all includes event $\mathcal{R}_4$. The visual inspection of Figure 10 leads to the following explanation. If event $\mathcal{R}_4$ is present, as in submodel $(\mathcal{R}_1, \mathcal{R}_4)$, the proliferative cells can keep dividing after the extinction of the precursor cells (line $f = 0$). Once the precursor cell number reaches zero for a given c, all remaining points $(0, c')$ for $c' \geq c$ are reached with probability one, which results in a comparatively low contribution of all $(0, c)$ data points to the negative log-likelihood. In contrast, if event $\mathcal{R}_4$ is not present, as in submodel $(\mathcal{R}_1, \mathcal{R}_3)$, the process stops as soon as the precursor cell population F gets extinct, which prevents the likelihood of all $(0, c')$ points from being close to one (they rather take all intermediate values).

	Wild-Type			Mutant		
Model	-log $\mathcal{L}(\theta; \mathbf{x})$	AIC	BIC	-log $\mathcal{L}(\theta; \mathbf{x})$	AIC	BIC
$(\mathcal{R}_1, \mathcal{R}_4)$	172.87	349.74 $w = 0.02$ $\Delta = 7.6$	354.74 $w = 0.15$ $\Delta = 3.0$	149.97	303.94 $w = 0.08$ $\Delta = 8.8$	308.73 $w = 0.03$ $\Delta = 6.4$
$(\mathcal{R}_1, \mathcal{R}_3)$	245.54	495.09 $w < 10^{-10}$ $\Delta >> 10$	500.09 $w < 10^{-10}$ $\Delta >> 10$	230.17	464.34 $w < 10^{-10}$ $\Delta >> 10$	469.13 $w < 10^{-10}$ $\Delta >> 10$
$(\mathcal{R}_1, \mathcal{R}_2, \mathcal{R}_4)$	172.77	351.54 $w = 0.008$ $\Delta = 9.44$	359.04 $w < 10^{-10}$ $\Delta = 7.4$	148.14	302.27 $w = 0.02$ $\Delta = 7.1$	309.46 $w = 0.02$ $\Delta = 7.1$
$(\mathcal{R}_1, \mathcal{R}_2, \mathcal{R}_3)$	242.51	491.02 $w < 10^{-10}$ $\Delta >> 10$	498.52 $w < 10^{-10}$ $\Delta >> 10$	229.44	464.89 $w < 10^{-10}$ $\Delta >> 10$	472.07 $w < 10^{-10}$ $\Delta >> 10$
$(\mathcal{R}_1, \mathcal{R}_3, \mathcal{R}_4)$	170.58	347.16 $w = 0.07$ $\Delta = 5.0$	354.66 $w = 0.15$ $\Delta = 3.0$	144.58	295.15 $w = 0.64$	302.34 $w = 0.81$
$(\mathcal{R}_i)_{i \in [\![1,4]\!]}$	167.05	342.10 $w = 0.90$	351.68 $w = 0.68$	144.24	296.48 $w = 0.33$ $\Delta = 1.3$	306.06 $w = 0.12$ $\Delta = 3.7$

Table 2 Model comparison analysis. For each experimental subset and each submodel, we compute both the Akaike information criterion (AIC) and Bayesian information criterion (BIC), the AIC and BIC differences $\Delta_i^{AIC} := AIC_i - AIC_{\min}$ and $\Delta_i^{BIC} = BIC_i - BIC_{\min}$, and the corresponding Akaike and Bayesian weights $w_i^{AIC} = \frac{\exp(-0.5\Delta_i^{AIC})}{\sum_{k=1}^{6} \exp(-0.5\Delta_k^{AIC})}$ and $w_i^{BIC} = \frac{\exp(-0.5\Delta_i^{BIC})}{\sum_{k=1}^{6} \exp(-0.5\Delta_k^{BIC})}$ following the formulas provided in Burnham and Anderson (2003) (Chapter 2 and 3).

4.4 Model prediction

In this subsection, we use the fitted parameter sets $\hat{\theta}^l_m$ and the parameter values $\hat{\theta}^l_m|\hat{\theta}^l_{m,i}$, for which the PLE is below the 95% threshold of the best models (the two linear submodels $(\mathcal{R}_1, \mathcal{R}_4)$ and $(\mathcal{R}_1, \mathcal{R}_3, \mathcal{R}_4)$ and the complete model) to infer information on the experimental subsets.

4.4.1 Distribution of the initial condition

In the previous section, we have observed that the initial condition parameter μ is the unique parameter to be practically identifiable in all cases, and that it is fitted to similar values from one submodel to another (see Table 2). Parameter μ can be either estimated from the whole experimental subsets, as the other parameters, or, alternatively, from the cell number of the primordial follicles only. For all $l \in \mathbf{B}$, let $\mathbf{x}^l_{ini}$ be the subset composed of the sole primordial follicles:

$$\mathbf{x}^l_{ini} := \{(f_i, c_i) \in \mathbf{x}^l \text{ such that } c_i = 0, i \in [\![1, N^l]\!]\}.$$

We recall here that F_0 is assumed to follow a truncated Poisson law of parameter μ (see Eq. (47)). We use again a classical maximum likelihood approach, associated with the experimental dataset $\mathbf{x}^l_{ini}$. From the likelihood function

$$\mathcal{L}_{ini}(\mathbf{x}^l_{ini}; \mu) := \prod_{i \in [\![1, N^l]\!] : c_i = 0} \frac{\mu^{f_i}}{(e^\mu - 1) f_i!},$$

we deduce the MLE $\hat{\mu}^l_{ini}$, for all $l \in \mathbf{B}$,

$$\hat{\mu}^l_{ini} := \arg\min_{\mu \geq 1} \left(-\log \left(\mathcal{L}_{ini}(\mathbf{x}^l_{ini}; \mu) \right) \right).$$

The law F_0 with parameter $\hat{\mu}^l_{ini}$ is thus inferred solely from the primordial follicle data, while the law F_0 with parameter $\hat{\mu}^l$ is inferred using also the transitory and primary follicle data.
In Figure 14, we compare for each subset WT or M the distributions derived from model $(\mathcal{R}_1, \mathcal{R}_4)$, $(\mathcal{R}_1, \mathcal{R}_3, \mathcal{R}_4)$ and $(\mathcal{R}_1, \mathcal{R}_2, \mathcal{R}_3, \mathcal{R}_4)$, using either only the primordial follicle data or the complete follicle data. From the top panels of Figure 14, we observe that in all cases, there is an overestimation of the part of the distribution corresponding to $\mathbb{P}[F_0 \leq 5]$, which suggests that the model for the initial condition should be a more truncated Poisson distribution for the low values of F_0. As expected, using more information leads to narrowing down the uncertainties, hence the confidence intervals are smaller when the whole data are used (for all models and subsets considered). More surprisingly, we observe a shift of approximately one cell in average, in opposite directions for the Wild-Type and Mutant subset: for the Wild-Type subset, the mean cell number is found to be greater when the whole data are used, while for the Mutant subset, the mean cell number is found to be smaller (for all three models considered). In details, the confidence intervals for the Mutant subset

using the whole data superimposes totally or partially to the confidence intervals using only the primordial follicle data, with an overlap of 100% for model $(\mathcal{R}_1, \mathcal{R}_4)$, 65% for model $(\mathcal{R}_1, \mathcal{R}_2, \mathcal{R}_3, \mathcal{R}_4)$, and 50% for model $(\mathcal{R}_1, \mathcal{R}_3, \mathcal{R}_4)$. In the Wild-Type subset, the confidence intervals are more disjoint, with an overlap of 64% for model $(\mathcal{R}_1, \mathcal{R}_2, \mathcal{R}_3, \mathcal{R}_4)$, 25% for model $(\mathcal{R}_1, \mathcal{R}_3, \mathcal{R}_4)$, and no overlap at all for model $(\mathcal{R}_1, \mathcal{R}_4)$.

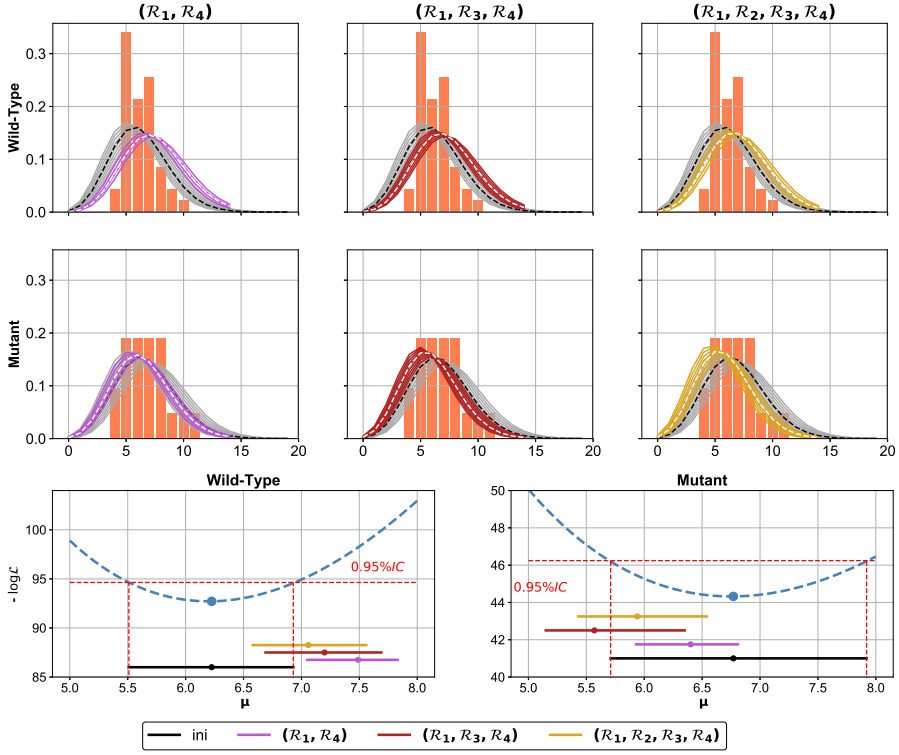

Fig. 14 Initial condition. Top and middle panels: experimental data histograms of the number of precursor cells in primordial follicles with inferred Poisson distributions. Histograms with coral-colored bars: initial precursor cell number in primordial follicles for Wild-Type x_{ini}^{WT} (top panels) and Mutant x_{ini}^{M} (middle panels) subsets. For subsets $l \in \mathbf{B}$ and submodels $(\mathcal{R}_1, \mathcal{R}_4)$ (left panels), $(\mathcal{R}_1, \mathcal{R}_3, \mathcal{R}_4)$ (center panels) and $(\mathcal{R}_1, \mathcal{R}_2, \mathcal{R}_3, \mathcal{R}_4)$ (right panels), we plot: in white dashed lines, the truncated Poisson distribution (47) with MLE $\hat{\mu}_m^l$; in colored solid lines: the truncated Poisson distribution (47) with μ in the confidence interval of $\hat{\mu}_m^l$; in black dashed lines: the truncated Poisson distribution (47) with MLE $\hat{\mu}_{ini}^l$; in gray solid lines, the truncated Poisson distribution (47) with μ in the confidence interval of $\hat{\mu}_{ini}^l$ (parameter values: $\hat{\mu}_{ini}^{WT} = 6.22 \in [5.54; 6.67]$, $\hat{\mu}_{ini}^{M} = 6.77 \in [5.75; 7.60]$). Bottom panels: negative log-likelihood function $\mathcal{L}_{ini}(\mathbf{x}_{ini}^l; \mu)$ and confidence intervals of $\hat{\mu}_{ini}^l$ and $\hat{\mu}_m^l$ (left panel: Wild-Type, right panel: Mutant). Cyan dashed lines: log-likelihood function $\mathcal{L}_{ini}(\mathbf{x}_{ini}^l; \mu)$; red dashed lines: 95% confidence interval; colored solid lines (resp. filled circles): confidence intervals of $\hat{\mu}_m^l$ (resp. $\hat{\mu}_m^l$ values) for each submodel.

4.4.2 Proliferative cell proportion: reconstruction of time

In Figure 15, we represent the predicted change in the proliferative cell proportion with respect to time. These predictions are derived from the deterministic formula Eq. (7) for each model, using the parameter values obtained from the identifiability analysis, for which the PLE is below the 95% threshold. In both the Wild-Type and Mutant cases, despite the uncertainty affecting the model parameters for the two linear submodels (left and right upper panels), the dynamics just exhibit small uncertainties: the proportion of proliferative cells reaches 50%-70% in one time unit, which corresponds to the time unit of a single spontaneous transition event. This might due partly to the fact that parameter γ is partially identifiable and is estimated to relatively low values. In contrast, the lack of parameter identifiability of the complete model results in a huge uncertainty on the dynamics, that can be up to 5 order of magnitude faster than a single spontaneous transition event: the proportion of proliferative cells reaches 50% between 10^{-6} and 1 time unit. Indeed, cell event $\mathcal{R}_2$ (controlled by parameter β_1) can speed up the transition dynamics, and cell event $\mathcal{R}_3$ (controlled by parameter α_2) can trigger the transition, leading to a possible fast activation which avoids the bottleneck of the spontaneous transition timescale ($\alpha_1 = 1$). No clear timescale separation between the Wild-type and Mutant dynamics can be revealed, although some parameter combinations are compatible with a faster transition in the Wild-Type case than in the Mutant case.

4.4.3 Mean extinction time, mean number of cells at the extinction time and mean number of division events before extinction

In Figure 16, we represent the mean number of proliferative cells, $\mathbb{E}\left[C_{\tau^{F_0}}\right]$, as a function of the extinction time $\mathbb{E}\left[\tau^{F_0}\right]$, and the mean number of division events before extinction, $\mathbb{E}\left[C_{\tau^{F_0}} - F_0\right]$, as predicted from the selected (sub)models $(\mathcal{R}_1, \mathcal{R}_4)$, $(\mathcal{R}_1, \mathcal{R}_3, \mathcal{R}_4)$ and $(\mathcal{R}_1, \mathcal{R}_2, \mathcal{R}_3, \mathcal{R}_4)$. These predictions are obtained from a direct stochastic simulation of the trajectories of each model (with Gillespie algorithm, or SSA)[1], using the parameter values obtained from the identifiability analysis, for which the PLE is below the 95% threshold. For each subset (Wild-Type or Mutant), the predicted mean number of proliferative cells at the extinction time is similar in each submodels and lies between 8 and 10 cells. Interestingly, the predicted mean number of proliferative cells at the extinction time is approximately 6-8 cells lower than the empirical mean number of proliferative cells obtained directly from the primary follicle data set $\{x^l,\ \text{such that}\ f = 0\}$ (Figure 16, top panels). This observation is consistent with the trajectory analysis performed from Figure 10 for submodel $(\mathcal{R}_1, \mathcal{R}_4)$

[1] We use here the direct simulation rather than Algorithm 1, because the parameter range explored by the symmetric division rate γ in the PLE exceeds the bound $\gamma < \alpha_1$ required by Algorithm 1. A finer upper-bound of the proliferative cell population in the nonlinear process (taking into account event $\mathcal{R}_2$ for instance) would be required to use a finite state projection method when $\gamma > \alpha_1$.

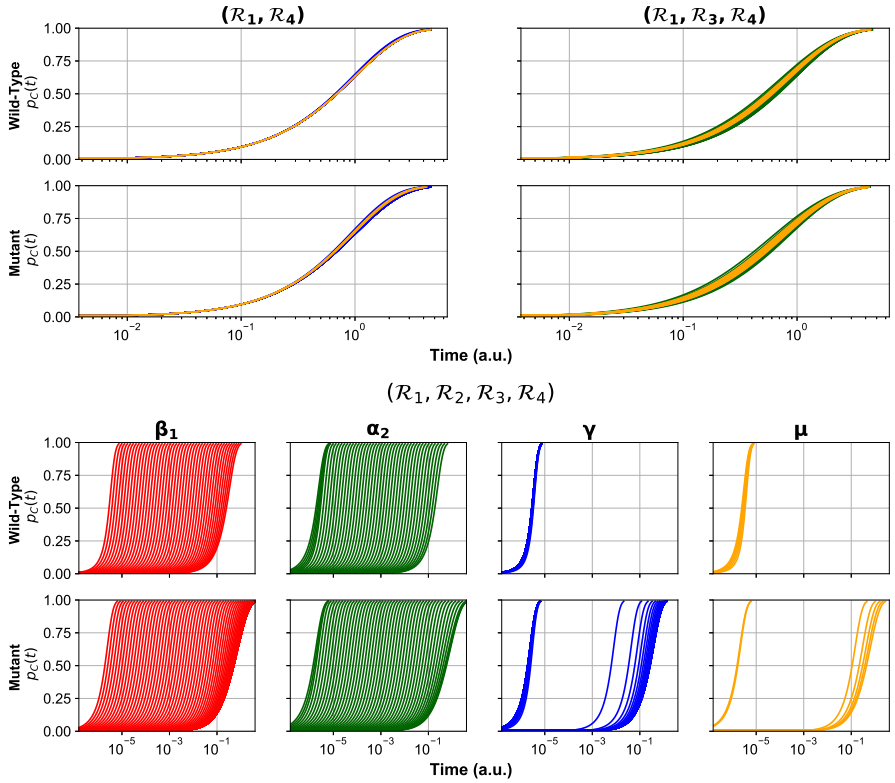

Fig. 15 Dynamics of the proportion of proliferative cells. For submodel $(\mathcal{R}_1, \mathcal{R}_4)$ (top left panels), $(\mathcal{R}_1, \mathcal{R}_3, \mathcal{R}_4)$ (top right panels) and whole model $(\mathcal{R}_1, \mathcal{R}_2, \mathcal{R}_3, \mathcal{R}_4)$: $(\mathcal{R}_1, \mathcal{R}_3)$ (bottom panels), we plot the deterministic proportion of proliferative cells $p_C(t)$ computed from Eq. (7) with the fitted parameters lying in the MLE confidence interval $\hat{\theta}_m^l$ associated with each profile likelihood (see subsection 4.2 for details). Blue lines: $p_C(t)$ with parameters $\hat{\theta}_m^l|\gamma$; yellow lines: $p_C(t)$ with parameters $\hat{\theta}_m^l|\mu$; green lines: $p_C(t)$ with parameters $\hat{\theta}_m^l|\alpha_2$; red lines: $p_C(t)$ with parameters $\hat{\theta}_m^l|\beta_1$.

and Figure 13 for the complete model, from which we have concluded that the activation process follows with high probability a trajectory reaching state $f = 0$ with a low cell number, and characterized by direct transition and very little concomitant cell proliferation.

Similarly, the mean number of division events before the extinction time is approximately 5-7 cells lower than the increase in the mean empirical number of cells between the primordial follicle datasets and primary follicle datasets (Figure 16, bottom panels). The mean extinction time of the two linear submodels $(\mathcal{R}_1, \mathcal{R}_4)$ and $(\mathcal{R}_1, \mathcal{R}_3, \mathcal{R}_4)$ depends only on the initial condition and is estimated to a value around 2.5 a.u. with a small uncertainty, similarly as in Figure 15. In contrast, the complete model yields a larger uncertainty on the mean extinction time, with a confidence interval between 10^{-6} and 0.5 a.u. for the Wild-Type subset, and between 10^{-6} and 2.5 a.u. for the Mutant

subset, consistently with the prediction on the dynamics of the proliferative cell proportion (Figure 15).

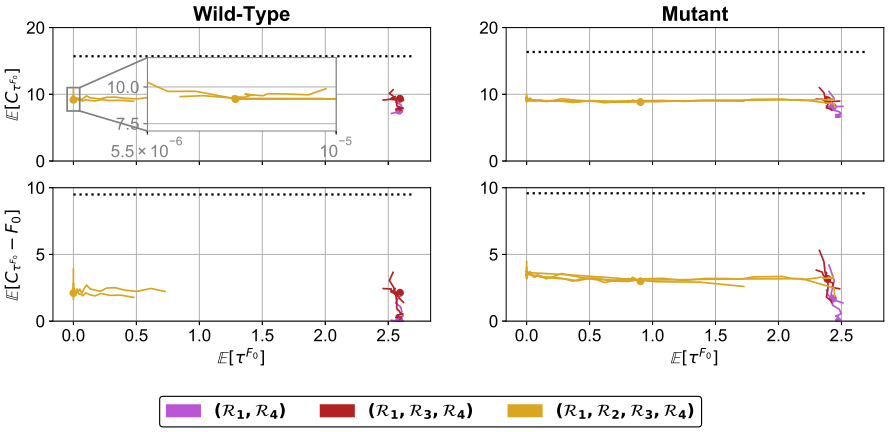

Fig. 16 Prediction of the mean number of proliferative cells and mean number of division events before extinction. We plot the mean number of proliferative cells at the extinction time $\mathbb{E}\left[C_\tau^{F_0}\right]$ (top panels), and the mean number of division events before extinction $\mathbb{E}\left[C_\tau^{F_0} - F_0\right]$ (bottom panels) as a function of the mean extinction time $\mathbb{E}\left[\tau^{F_0}\right]$ (left panels: Wild-Type; right panels: Mutant). For each parameter lying in the MLE confidence interval$\hat{\theta}_m^l$, we simulate 10,000 trajectories with the Gillespie algorithm, up to the extinction event $\{F = 0\}$, and compute $\mathbb{E}\left[\tau^{F_0}\right]$, $\mathbb{E}\left[C_\tau^{F_0}\right]$ and $\mathbb{E}\left[C_\tau^{F_0} - F_0\right]$ from standard empirical mean estimates. Colored solid lines: $\mathbb{E}\left[C_\tau^{F_0}\right]$, $\mathbb{E}\left[C_\tau^{F_0} - F_0\right]$ as a function of $\mathbb{E}\left[\tau^{F_0}\right]$ for parameters $\hat{\theta}_m^l | p$ and $p \in \{\beta_1, \alpha_2, \gamma, \mu\}$ associated with each profile likelihood (see subsection 4.2 for details); filled circles: $\hat{\theta}_m^l$, for submodels $\{(\mathcal{R}_1, \mathcal{R}_4)$, $(\mathcal{R}_1, \mathcal{R}_3, \mathcal{R}_4)$, and complete model $(\mathcal{R}_1, \mathcal{R}_2, \mathcal{R}_3, \mathcal{R}_4)\}$. Dotted black lines: standard empirical mean estimate of proliferative cell numbers (top panels) and division events (bottom panels) before extinction in the primary follicles (data set $\{x^l$, such that $f = 0\}$).

4.4.4 Biological interpretation

From the primordial follicle data, we have found that the mean initial number of precursor cells $\hat{\mu}_{ini}^{WT}$ for the Wild-Type subset is about the same as $\hat{\mu}_{ini}^{M}$ for the Mutant. Moreover, the prediction on the total number of proliferative cells at the end of the activation phase, $\mathbb{E}\left[C_\tau^{F_0}\right]$, is also very similar in the Wild-Type and Mutant cases. The observed shift in opposite directions for the mean initial cell number inferred from the MLE of the dynamical models ($\hat{\mu}_m^{WT} \approx \hat{\mu}_{ini}^{WT} + 1$ and $\hat{\mu}_m^{M} \approx \hat{\mu}_{ini}^{M} - 1$) is thus compensated for by the differences in cell dynamics. The number of divisions during the transition is smaller in the Wild-Type than in the Mutant subset ($\mathbb{E}[C_\tau - F_0] \approx 2$ in Wild-Type, $\mathbb{E}[C_\tau - F_0] \approx 4$ in Mutant), as a result of a global difference between the MLE parameters: the order of magnitude of the division rates are closer to that of the

transition rates in the Mutant compared to the Wild-Type subset. In overall, we conclude from our extensive datafitting analysis that the Wild-Type subset exhibits a clearer separation of dynamics during follicle activation (first cell transition, then cell proliferation), while in the Mutant cell proliferation could occur at a substantial rate before precursor cell extinction. We note that this conclusion has to be tempered by the sparse character of our experimental dataset. In particular, a detailed examination of the experimental data reveals that the four data points available for transitory follicles in the Wild-Type subset correspond to a clearly higher number of precursor cells than any of the primordial follicles, which certainly impacts our results. In contrast, the Mutant subset contains transitory follicles with significantly fewer precursor cells than the primary follicles.

Finally, we highlight that the β_1-free linear submodel $(\mathcal{R}_1, \mathcal{R}_3, \mathcal{R}_4)$ performs as well as, and even better than the complete model $(\mathcal{M}_{FC})$ $(\mathcal{R}_i)_{i\in[\![1,4]\!]}$ in Mutant compared to Wild-Type ewes, which is compatible with the functional hypotheses applicable to the BMP15R mutation. Indeed, one could speculate that the diminished BMP15 signaling would hamper the molecular dialog between the oocyte and somatic cells after follicle activation triggering, so that the auto-amplified cell event would barely occur in the Mutant group.

5 Conclusion

In this work, we have introduced a stochastic nonlinear cell population model to study the sequence of events occurring just after the initiation of follicle growth. We have characterized the dynamics of precursor and proliferative cell populations according to the parameter values, for both the stochastic model and its deterministic mean-field counterpart. We have studied in details the extinction time of the precursor cell population, and designed an algorithm to compute numerically both the mean extinction time and mean number of proliferative cells at the extinction time. The algorithm is based on a domain truncation similar to the Finite State Projection (FSP) method proposed in Munsky and Khammash (2006); Kuntz (2017). The FSP approach aims to approximate the law of the process at a given time by solving a truncated version of the Kolmogorov forward system. We have adapted the FSP algorithm to solve the infinite recurrence relation satisfied by the extinction time moments. We have found a consistent spatial boundary to solve the closure problem, thanks to a coupling technique and tractable upper-bound process. The numerical cost of the algorithm is deeply related to the proper choice of the upper-bound processes. As we have noticed in section 4, a finer approximation would be required to compute the mean extinction time and mean number of proliferative cells at the extinction time using the FSP method when dealing with a broader range of parameters (and in particular the case $\alpha_1 < \gamma < \beta_1$).

This algorithm has nevertheless allowed us to investigate the parameter influence on the precursor cell extinction time and number of proliferative cells at the end of the follicle activation phase. The auto-amplified transition

rate β_1 exerts a critical control on the mean extinction time, with a sharp timescale reduction when β_1 exceeds the spontaneous cell transition α_1, while the division rates (α_2, γ) have relatively less effect. The effect of the auto-amplification process is probably dependent on the specific parameterization of the cell event rates chosen in this work, yet our findings bring interesting insight into the mechanisms underlying follicle activation; nonlinear feedbacks mediated through cell-to-cell communication certainly play a role, and our estimation results have shown that any impairment of this feedback would change drastically the kinetics of follicle activation.

Moreover, our results can be useful to understand the variability in the cell numbers among ovarian follicles at the end of the activation phase, which can be used as initial conditions for models describing the following stages of follicle development Clément et al. (2013, 2019).

We have performed the parameter calibration in a special context of time-free data. It turns out that the proliferative cell dynamics can be seen as a clock for the whole process, and that the embedded Markov chain is better adapted to the time-free data than the continuous-time model. We have used the embedded Markov chain to define a proper likelihood function and a statistically rigorous framework. The likelihood function has allowed us to perform an extensive data fitting analysis, using the very useful concept of profile likelihood estimate. This analysis sheds light onto several aspects of the activation of ovarian follicles. First, the transition scenario, where cell proliferation is mostly posterior to cell transition, and the cell number increase is moderate, seems to be predominant versus a more proliferative scenario. While the question is still open, it seems likely that cell transition is favored in the Wild-Type strain compared to the Booroola mutant strain. With the available experimental dataset, we have yet not managed to make a clear distinction between, on one side, a progressive transition with a steady net flux from flattened to cuboidal cells, and, on the other side, an auto-catalytic transition with an ever increasing flux all along the activation phase.

Beyond our application in female reproductive biology, we believe that the modeling approach presented here can have a more generic interest in cell kinetics related issues, especially when a small number of cells is involved. Also, from the mathematical biology viewpoint, the analysis performed on the extinction time, combining theoretical (coupling) and numerical (finite state projection) tools may have an interest for first passage time studies in stochastic processes.

6 Appendix

6.1 MLE parameter sets

Model	β_1	α_2	γ	μ
$(\mathcal{R}_1, \mathcal{R}_4)$	/	/	10^{-6} $\in (0; 0.12]$	7.49 $\in [7.05; 7.83]$
$(\mathcal{R}_1, \mathcal{R}_3)$	/	1.18 $\in [0.67; 1.57]$	/	7.22 $\in [6.81; 7.83]$
$(\mathcal{R}_1, \mathcal{R}_2, \mathcal{R}_4)$	$10^6 \in \mathbb{R}$	/	$10^{4.35}$ $\in (0; 10^{5.03}]$	7.45 $\in [7.05; 7.83]$
$(\mathcal{R}_1, \mathcal{R}_2, \mathcal{R}_3)$	10^6 $\in [1.52; +\infty)$	$10^{5.75}$ $\in [2.00; 10^{5.88}]$	/	7.07 $\in [5.15; 6.35]$
$(\mathcal{R}_1, \mathcal{R}_3, \mathcal{R}_4)$	/	0.27 $\in [0.022; 0.52]$	10^-6 $\in (0; 0.068]$	7.20 $\in [6.69; 7.69]$
$(\mathcal{R}_1, \mathcal{R}_2, \mathcal{R}_3, \mathcal{R}_4)$	10^6 $\in [4.64; +\infty)$	$10^{4.78}$ $\in [0.87; 10^{5.27}]$	10^{-6} $\in (0; 10^{4.67}]$	7.06 $\in [6.58; 7.56]$

Table 3 Wild-Type parameter sets

Model	β_1	α_2	γ	μ
$(\mathcal{R}_1, \mathcal{R}_4)$	/	/	0.14 $\in (0; 0.28]$	6.40 $\in [5.93; 6.81]$
$(\mathcal{R}_1, \mathcal{R}_3)$	/	1.63 $\in [1.26; 2.20]$	/	5.91 $\in [5.34; 6.35]$
$(\mathcal{R}_1, \mathcal{R}_2, \mathcal{R}_4)$	10^6 $\in \mathbb{R}$	/	$10^{5.11}$ $\in [0.12; 10^{5.39}]$	6.26 $\in [5.72; 6.81]$
$(\mathcal{R}_1, \mathcal{R}_2, \mathcal{R}_3)$	10^6 $\in \mathbb{R}$	10^6 $\in [1.52; +\infty)$	/	5.57 $\in [5.15; 6.35]$
$(\mathcal{R}_1, \mathcal{R}_3, \mathcal{R}_4)$	/	0.52 $\in [0.21; 0.91]$	10^{-6} $\in (0, 0.98]$	5.94 $\in [5.43; 6.54]$
$(\mathcal{R}_1, \mathcal{R}_2, \mathcal{R}_3, \mathcal{R}_4)$	2.81 $\in \mathbb{R}_+$	1.16 $\in [0.28; 10^{5.51}]$	10^{-6} $\in (0; 10^{4.9}]$	5.83 $\in [5.15; 6.35]$

Table 4 Mutant parameter sets

Model	Parameter	Wild-Type/Mutant	Dataset $\mathbf{x}_1^{\cdot}$	Dataset $\mathbf{x}_2^{\cdot}$
$(\mathcal{R}_1, \mathcal{R}_4)$	μ	0.015	0.005	0.01
	γ	0.12	0.01	0.06
$(\mathcal{R}_1, \mathcal{R}_3)$	μ	0.015	0.005	0.005
	α_2	0.04	0.01	0.01
$(\mathcal{R}_1, \mathcal{R}_2, \mathcal{R}_4)$	μ	0.015	0.01	0.015
	β_1	0.12	0.07	0.12
	γ	0.12	0.07	0.12
$(\mathcal{R}_1, \mathcal{R}_2, \mathcal{R}_3)$	μ	0.015	0.015	0.015
	β_1	0.12	0.12	0.12
	α_2	0.12	0.02	0.02
$(\mathcal{R}_1, \mathcal{R}_3, \mathcal{R}_4)$	μ	0.01	0.01	0.01
	α_2	0.08	0.01	0.01
	γ	0.08	0.01	0.01
$(\mathcal{R}_1, \mathcal{R}_2, \mathcal{R}_3, \mathcal{R}_4)$	μ	0.015	0.015	0.015
	β_1	0.12	0.12	0.12
	α_2	0.12	0.12	0.12
	γ	0.12	0.12	0.12

Table 5 PLE parameter size-step

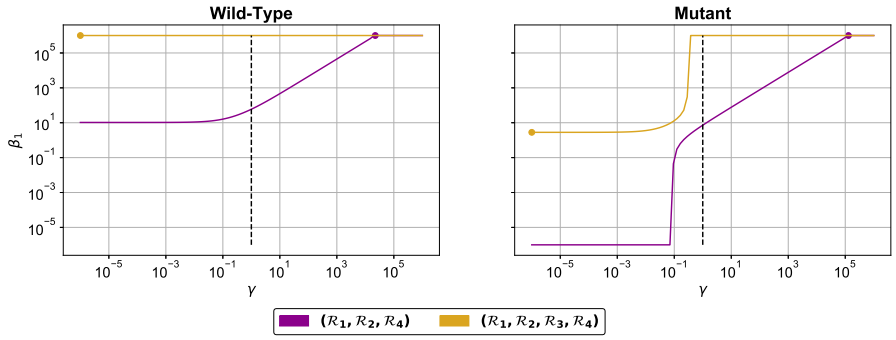

Fig. 17 Proliferation versus transition. For each subset (Wild-Type and Mutant), and for submodel $(\mathcal{R}_1, \mathcal{R}_2, \mathcal{R}_4)$ and complete model $(\mathcal{R}_1, \mathcal{R}_2, \mathcal{R}_3, \mathcal{R}_4)$, we represent the optimal value of β_1 along the PLE of γ, $(\widehat{\beta_1})^{l}_{m}|\gamma$ (the PLE of γ is given by the blue lines in the top panels of Figure 12 and bottom panels of Figure 13).

Acknowledgements The authors wish to thank Ken McNatty for providing the experimental dataset and Danielle Monniaux for helpful discussions.

References

Anderson DF, Kurtz TG (2015) Stochastic analysis of biochemical systems, vol 1. Springer

Braw-Tal R, Yossefi S (1997) Studies in vivo and in vitro on the initiation of follicle growth in the bovine ovary. J Reprod Fertil 109(1):165–171

Brémaud P (2013) Markov chains: Gibbs fields, Monte Carlo simulation, and queues, Texts in Applied Mathematics, vol 31. Springer Science & Business Media

Burnham K, Anderson D (2003) Model selection and multimodel inference: a practical information theoretic approach, 2nd edn. Springer-Verlag New York

Castro M, López-García M, Lythe C, Molina-París C (2018) First passage events in biological systems with non-exponential inter-event times. Sci Rep 8(1):15054, DOI 10.1038/s41598-018-32961-7

Chou T, D'Orsogna M (2014) First passage problems in biology. In: First-passage phenomena and their Applications, World Scientific, pp 306–345, DOI https://doi.org/10.1142/9789814590297_0013

Clément F, Michel P, Monniaux D, Stiehl T (2013) Coupled somatic cell kinetics and germ cell growth: Multiscale moded-base insight on ovarian follicular development. Multiscale Model Simul 11:719–746, DOI 10.1137/120897249

Clément F, Robin F, Yvinec R (2019) Analysis and calibration of a linear model for structured cell populations with unidirectional motion: Application to the morphogenesis of ovarian follicles. SIAM J Appl Math 79(1):207–229, DOI 10.1137/17M1161336

Da Silva-Buttkus P, Jayasooriya G, Mora J, Mobberley M, Ryder T, Baithun M, Stark J, Franks S, Hardy K (2008) Effect of cell shape and packing density on granulosa cell proliferation and formation of multiple layers during early follicle development in the ovary. J Cell Sci 121(23):3890–3900, DOI 10.1242/jcs.036400

Darling R, Siegert A (1953) The first passage problem for a continuous markov process. Ann Math Statist 24(4):624–639

Fortune J (2003) The early stages of follicular development: activation of primordial follicles and growth of preantral follicles. Anim Reprod Sci 78(3):135 – 163, DOI 10.1016/S0378-4320(03)00088-5, URL `http://www.sciencedirect.com/science/article/pii/S0378432003000885`

Freret-Hodara B, Cui Y, Griveau A, Vigier L, Arai Y, Touboul J, Pierani A (2016) Enhanced abventricular proliferation compensates cell death in the embryonic cerebral cortex. Cereb Cortex 27(10), DOI 10.1093/cercor/bhw264

Getto P, Marciniak-Czochra A (2015) Mathematical modelling as a tool to understand cell self-renewal and differentiation. Methods Mol Biol 1293:247–266, DOI 10.1007/978-1-4939-2519-3_15

Gillespie D (1976) A general method for numerically simulating the stochastic time evolution of coupled chemical reactions. J Comput Phys 22(4):403–434, DOI 10.1016/0021-9991(76)90041-3

Gillespie D (2001) Approximate accelerated stochastic simulation of chemically reacting systems. J Chem Phys 115(4):1716–1733

Glauche I, Cross M, Loeffler R, Roeder I (2007) Lineage specification of hematopoietic stem cells: mathematical modeling and biological implications. Stem Cells 25(7):1791–1799

Gougeon A, Chainy G (1987) Morphometric studies of small follicles in ovaries of women at different ages. J Reprod Fertil 81(2):433–442

Gratie DE, Iancu B, Petre I (2013) ODE analysis of biological systems. In: Formal Methods for Dynamical Systems, Springer, pp 29–62

Harris T (1963) The theory of branching processes. CRC Press, Berlin

Kimmel M, Axelrod D (2015) Branching processes in biology. 19, Springer-Verlag, DOI 10.1007/978-1-4939-1559-0

Knight P, Glister C (2006) TGF-beta superfamily members and ovarian follicle development. Reproduction 132(2):191–206

Kuntz J (2017) Deterministic approximation schemes with computable errors for the distributions of markov chains. Phd thesis, Imperial College London

Lundy T, Smith P, O'connell A, Hudson N, McNatty K (1999) Populations of granulosa cells in small follicles of the sheep ovary. J Reprod Fertil 115(2):251–262

Marr C, Strasser M, Schwarzfischer M, Schroeder T, Theis F (2012) Multi-scale modeling of GMP differentiation based on single-cell genealogies. FEBS J 279(18):3488–500, DOI doi:10.1111/j.1742-4658.2012.08664.x

Meredith S, Dudenhoeffer G, Jackson K (2000) Classification of small type B/C follicles as primordial follicles in mature rats. J Reprod Fertil 119(1):43–48

Monniaux D (2016) Driving folliculogenesis by the oocyte-somatic cell dialog: Lessons from genetic models. Theriogenology 86(1):41–53, DOI 10.1016/j.theriogenology.2016.04.017

Monniaux D (2018) Factors influencing establishment of the ovarian reserve and their effects on fertility. Anim Reprod 15(Suppl.1):635–647, DOI 10.21451/1984-3143-AR2018-0011

Monniaux D, Cadoret V, Clément F, Dalbies-Tran R, Elis S, Fabre S, Maillard V, Monget P, Uzbekova S (2018) Folliculogenesis. In: Huhtaniemi I, Martini L (eds) Encyclopedia of Endocrine Diseases (Second Edition), Elsevier, pp 377–398, DOI 10.1016/B978-0-12-801238-3.64550-6

Munsky B, Khammash M (2006) The finite state projection algorithm for the solution of the chemical master equation. J Chem Phys 124(4):044104

Picton H (2001) Activation of follicle development: the primordial follicle. Theriogenology 55(6):1193 – 1210, DOI https://doi.org/10.1016/S0093-691X(01)00478-2

Pujo-Menjouet L (2016) Blood cell dynamics: half of a century of modelling. Math Model Nat Phenom 11(1):92–115, DOI 10.1051/mmnp/201611106

Raue A, Kreutz C, Maiwald T, Bachmann J, Schilling M, Klingmüller U, Timmer J (2009) Structural and practical identifiability analysis of partially observed dynamical models by exploiting the profile likelihood. Bioinformatics 25(15):1923–1929, DOI 10.1093/bioinformatics/btp358

Reader K, Haydon L, Littlejohn R, Juengel J, McNatty K (2012) Booroola BMPR1B mutation alters early follicular development and oocyte ultrastructure in sheep. Reprod Fertil Dev 24(2):353–361, DOI 10.1071/RD11095

Reddy P, Zheng W, Liu K (2010) Mechanisms maintaining the dormancy and survival of mammalian primordial follicles. Trends Endocrinol Metab

21(2):96–103, DOI 10.1016/j.tem.2009.10.001

Sawyer H, Smith P, Heath D, Juengel J, Wakefield S, McNatty K (2002) Formation of ovarian follicles during fetal development in sheep. Biol Reprod 66(4):1134–1150

Stiehl T, Marciniak-Czochra A (2017) Stem cell self-renewal in regeneration and cancer: Insights from mathematical modeling. Methods Mol Biol 5:112–120, DOI 10.1016/j.coisb.2017.09.006

Storn R, Price K (1997) Differential evolution – a simple and efficient heuristic for global optimization over continuous spaces. J Global Optim 11:341–359, DOI 10.1023/A:1008202821328, URL https://doi.org/10.1023/A:1008202821328

Van Kampen N (1992) Stochastic processes in physics and chemistry, vol 1. Elsevier

Wilkinson D (2011) Stochastic Modelling for Systems Biology, Second Edition. Texts in Applied Mathematics, CRC Press

Wilson T, Wu X, Juengel J, Ross I, Lumsden J, Lord E, Dodds K, Walling G, Mcewan J, O'connell A, Mcnatty K, Montgomery G (2001) Highly prolific booroola sheep have a mutation in the intracellular kinase domain of bone morphogenetic protein Ib receptor (Alk-6) that is expressed in both oocytes and granulosa cells. Biol Reprod 64(4):1225–1235

Zhang H, Risal S, Gorre N, Busayavalasa K, Li X, Shen Y, Bosbach B, Brännström M, Liu K (2014) Somatic cells initiate primordial follicle activation and govern the development of dormant oocytes in mice. Curr Biol 24(21):2501–2508, DOI 10.1016/j.cub.2014.09.023